

# Chapter 1 Introduction

## 1.1 Motivation

Twenty-five years ago, neurophysiology was revolutionized by the invention of a clever way to record the electric activity of a single ionic channel across a membrane [1]. This so-called patch-clamp technique earned its inventors, Erwin Neher and Bert Sakmann, a Nobel Prize. The statistical analysis of the current flowing like a noisy telegraphic signal through such a channel yielded precious and unique information on the dynamic states of these channels. That information had previously been blurred or lost when, as was the prior custom, one simply measured the average current flowing through a large ensemble of channels.

The biological research (such as in the fields of biophysics and cell biology) and biotechnology (drug screening and diagnostics applications) are undergoing a similar transformation, thanks to the development of new tools for non-invasive manipulation of micro- and nano- sized objects. The tool allows cells, cellular components, and synthetic marker particles treated with biochemical tags to be collected, separated, concentrated, and transported without damage to the objects themselves. Furthermore, it is possible to manipulate and study DNA, viruses and protein molecules, which are several orders of magnitude smaller than cells. In this way, a lot of new biological mechanism has been learned in recent years such as the mechanochemical coupling in the enzymes responsible for muscle contraction (actin and myosin), transport in the cell (kinesin and tubulin), energy generation (F1-ATPase), DNA replication and transcription (polymerase), DNA unknotting and unwinding (topoisomerases and helicases), and so on [2]. It is also expected to utilize the tool to separate all proteins from the human proteome, measure the genetic expression which could have numerous applications in drug screening and discovery, and even build an active artificial immune system in vitro [3].

For the past forty years, electronic computers have grown more powerful as their basic sub-unit, the transistor, has shrunk. However, the laws of quantum mechanics, plus the limitation of materials and fabrication techniques are likely to inhibit further reduction in the minimum size of today's semiconductor transistors. In order to continue the miniaturization of integrated circuits, it is likely that the present micron-scale or microelectronic devices will be replaced with new designs for devices at the nanometer scale using nanotubes as building blocks [4]. Yet, there are major difficulties that prevent the realization of carbon nanotube-based circuitry today. One issue is the separation of metallic from semiconducting single-walled carbon nanotubes (SWNTs) either by selective production or by after-growth separation schemes. Another important issue is the assembly of SWNTs into a nanoscale structure. The non-invasive manipulation capability provides electrical engineers a powerful tool for solving both the two issues. Separation of metallic from semiconducting SWNTs and simultaneous deposition of metallic bundles of SWNTs on electrical contacts have already been realized by using dielectrophoresis, which is one of the most important methods for non-invasive manipulation of micro/nano objects. The fabricated nanostructure shows the Schottky-barrier-type field-effect transistor with p-type, ambipolar or n-type behavior [5]. Recently using the similar method to achieve controlled alignment of an individual SWNT between electrical contacts is also reported [6].

Among various non-invasive manipulation mechanisms, a particularly desirable one is the ability to control the orientation of the objects, in addition to trapping and moving them. Such capability opens the door to building structured biomaterials for potential applications in constructing biofilms and human tissue engineering [7]. Organized cell structures such as artificial structured microbial consortia (ASMC) have already been created from cells of higher organisms by the technique with orientation control ability [8]. It is also expected to measure the characteristics of biological cells such as deformability, conformation states and physiological parameters through the orientation control approach which may have application in early diagnosis for diseases [9] [10]. It also suggests an ideal way to realize the artificial rotary machine in micro/nano scale. Such a rotary machine would be a step toward Drexler's vision of molecular nanotechnology [11], proving Feynman's statement that "there's plenty of room at the bottom" [12].

## 1.2 Opto-Plasmonic Tweezers

A new optical micro-manipulator and micro-rotator with low optical intensity requirement and fine orientation control ability is described in this thesis, called “Opto-Plasmonic Tweezers” which is depicted in Figure 1-1 [13]. In Figure 1-1, micro/nano objects with asymmetrical shapes are suspended in a solution. The light source, with its polarization adjusted by a fine polarization controller, has an electric-field component and is focused on a surface of the Au nanostructure. This electric field oscillates in time with frequency of the incident light, and induces the free electrons near the surface of the metal to move and form oscillating dipole moments. With a proper frequency, resonant oscillation of electrons can be induced, and localized surface plasmon resonance (LSPR) is formed. Such principle has already been applied to plasmonic waveguides in nano-scale photonics [14], targeted tumor treatment using metal nano-shells [15] and many other applications [16]. The direction of the oscillating dipoles is parallel to the electric-field polarization of the light. They radiate in the same way as oscillating charges, and create a patterned radiation electric field that manipulates the micro/nano objects through dielectrophoresis with fine orientation control by adjusting the polarization of the incident light. The detailed principle will be described in Chapter 3.

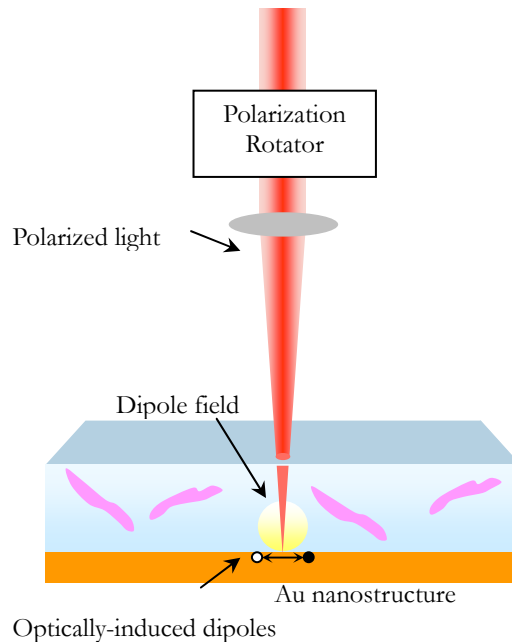


Figure 1-1 Manipulating micro/nano objects with orientation control by polarized light

Modeling based on physical principles of the proposed research, including localized surface plasmon excitation, dipole field radiation, and dielectrophoresis are created. The light induced dielectrophoresis forces on micro- and nano- spherical objects with known geometry and dielectric constants are examined. Subsequently, the trapping behavior under the dielectrophoresis force is simulated. The theoretical model is then expanded to simulate the dielectrophoretic force and torque on asymmetrical objects. Finally, *Listeria monocytogenes* is used as an example biological cell to simulate the optical manipulation and rotation of the cell. These contents will be discussed in Chapter 3.

For chapter 4, we turn to the fabrication and experiment. The Au nanoshell film is formed by using a layer of randomly adsorbed polystyrene spheres as a template. Au colloids in solution are also immobilized on the substrate by modifying the surface chemistry. The reflection and scattering spectrums of the two kinds of nanostructure are measured which show the resonance peak in visible range. Chapter 5 concludes the thesis with a discussion on the model results and fabrication process, as well as remarks on following works.

## Chapter 2 Prior Arts

Many approaches have been developed for the purpose of non-invasive manipulation of micro/nano objects using electrical, optical, mechanical and magnetic methods. Researchers have realized the manipulation of micro/nano objects in a large dimension range including colloids, cells, cellular components, latex beads, metal nanoparticles, DNA, viruses, proteins, nanotubes and nanowires.

### 2.1 Dielectrophoresis

In the past, dielectrophoresis (DEP) has been the most widely employed method for non-invasive manipulation of micro/nano objects. The discovery of dielectrophoresis goes all the way back to at least 600 B.C., when Thales of Miletus in Turkey observed the rubbed amber attracted small particles of fluff [17]. In retrospect the amber, being charged up from the rubbing, generated an electric field which polarized the fluff particles. The induced dipole in the fluff particles was acted on by the electric fields, attracting it to the charged amber. Today we would call this effect positive dielectrophoresis.

#### 2.1.1 Overview of dielectrophoresis

Consider a polarizable object exposed to an electric field. The applied electric field causes the formation of a dipole within the material and an accumulation of charge at the surface. If the electric field is uniform, the Coulomb forces on the charges on both sides of the object are equal and opposite, as are the forces on both sides; therefore, they cancel out and there is no net force on the object. However, if the field is non-uniform (that is, varying in magnitude across the region occupied by the particle), the Coulomb forces on either side will not be equal and there will be a net force on the object. This is called the dielectrophoretic force; the action of the movement by it is called dielectrophoresis [17, 18, 19].

Let us consider a spherical object in a non-uniform field such as the one shown in Figure 2-1. When this object is polarized, it will have centers of positive and negative charges that are equal in magnitude but separated by a distance  $d$  along vector  $r$ . Since the electric field is non-uniform, the positive and negative charges will experience different electric field strengths, giving rise to a total force on the object of

$$\bar{F} = Q^+ \bar{E}(r+d) - Q^- \bar{E}(r) \quad (1)$$

When  $d$  is small relative to the size of the electric field non-uniformity, we can approximate this as

$$\bar{E}(r+d) = \bar{E}(r) + d \cdot \bar{\nabla} E(r) \quad (2)$$

which allows us to rewrite the force as

$$\bar{F} = Q \bar{d} \cdot \bar{\nabla} E(r) \quad (3)$$

Since  $Q \bar{d}$  defines the dipole moment, the force can be written as

$$\bar{F} = (\bar{p} \cdot \bar{\nabla}) E \quad (4)$$

The general expression for DEP force on a spherical object is given by [18]:

$$\bar{F}_{DEP} = 2\pi\epsilon_m r^3 \operatorname{Re}\{f_{CM}(\omega)\} \bar{\nabla} |E_{RMS}|^2 \quad (5)$$

Where  $\epsilon_m$  is the real permittivity of the suspending medium,  $r$  is the radius of the spherical object,  $E_{RMS}$  is the root-mean-square (RMS) value of the imposed electric field (assuming a sinusoidal time dependence);  $\operatorname{Re}\{f_{CM}(\omega)\}$  is the real part of the *Clausius-Mossotti* factor which is related to the complex permittivities of the object and the medium  $\epsilon_p^*$  and  $\epsilon_m^*$  by

$$f_{CM}(\omega) \equiv \frac{(\epsilon_p^* - \epsilon_m^*)}{(\epsilon_p^* + 2\epsilon_m^*)} \quad (6)$$

For spherical objects, the *Clausius-Mossotti* factor can vary within the range of -0.5 to +1.0. When it is positive, objects move toward higher electric field regions, and this is termed positive dielectrophoresis. When it is negative, the objects move toward lower electric field regions, and this is termed negative dielectrophoresis. Both the positive and negative DEP force can be harnessed to move and manipulate polarizable micro-objects such as cells, marker particles suspended in liquid media. The non-uniform electric fields for these object manipulation and control operations are usually created by microelectrodes patterned on a substrate using fabrication techniques borrowed from MEMS (micro-electro-mechanical

systems) technology. A wide variety of structures, ranging from simple planar geometries to complex three-dimensional designs, have been under investigation [19].

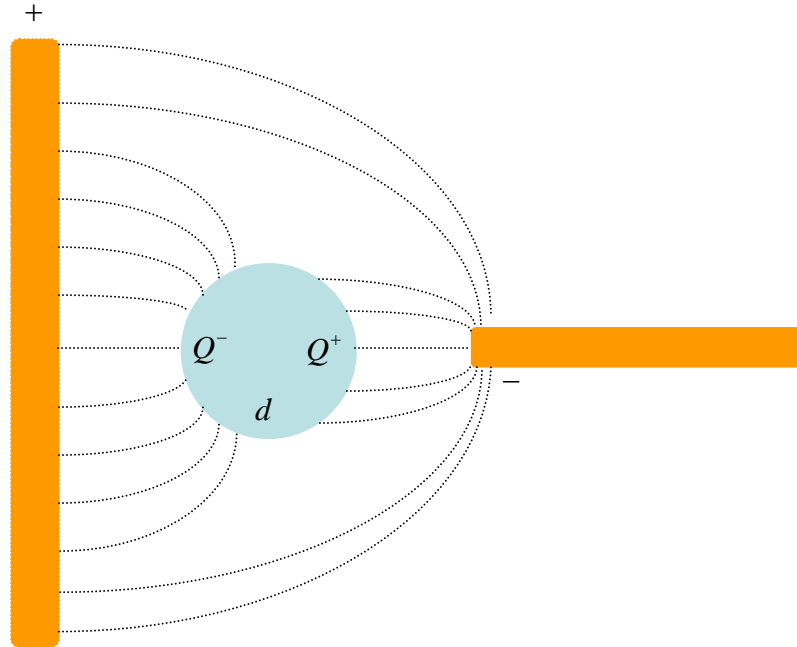


Figure 2-1 Dielectrophoresis occurs when a polarizable object is suspended in an electric field of non-uniform magnitude, so that the Coulombic forces induced on the charges on each half of the dipole are different.

### 2.1.2 Electrorotation

Consider the object in a rotating electric field generated by four electrodes with phase differences between their applied sinusoids shown in Figure 2-2. The electric field induces a dipole in the object as what happens for dielectrophoresis. However, as the field rotates, the dipole must keep up with it; if the dipole lags behind the electric field, the interaction between charges and field act to induce a torque (rotation force) on the object. Since the electric field is rotating continuously, the torque is constant and causes the object to rotate. The torque is at its minimum when the phase angle between the dipole and the applied field is zero, and it reaches its maximum when the phase angle is  $90^\circ$ . If the induced dipole moment lags behind the field, the direction of rotation is with the field and vice versa for a moment that leads the field [17, 18, 19].

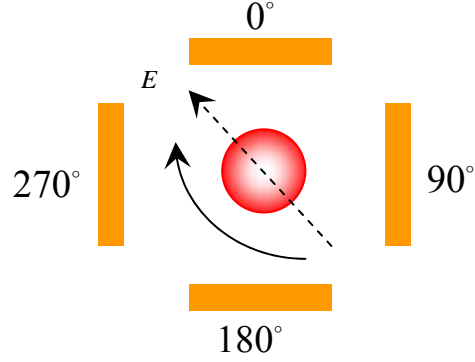


Figure 2-2 Electrorotation occurs when the object is placed in a rotating electric field

The torque exerted by an applied electric field on a dipole can be found by considering the net force acting about the center of a dipole, as before. The torque is given by

$$\vec{\Gamma} = \frac{\vec{d}}{2} \times Q\vec{E} + \frac{-\vec{d}}{2} \times (-Q\vec{E}) = Q\vec{d} \times \vec{E} \quad (7)$$

The general expression for electrorotational torque on a spherical object is given by [18]

$$\vec{\Gamma} = -4\pi\epsilon_m\epsilon_p r^3 \text{Im}\{f_{CM}(\omega)\} \vec{E}^2 \quad (8)$$

which depends on the imaginary part of the *Clausius-Mossoti* factor and the square of the field rather than its gradient. As with dielectrophoresis, there is an important connection between the direction of rotation and the value of  $\text{Im}\{f_{CM}(\omega)\}$ ; the direction of rotation is opposite to the direction of the rotating field when  $\text{Im}\{f_{CM}(\omega)\}$  is positive and in the same direction as the field when  $\text{Im}\{f_{CM}(\omega)\}$  is negative. These forms of rotation are referred to as co-field rotation and anti-field rotation, respectively. The fact that the direction is perhaps opposite to what one would expect is due to the presence of the minus sign. The physical reason for this effect relates to the fact that the displaced charges are repelled by like charges on the electrodes. Note also that since the field can interact with the charges to repel as well as rotate the object, it can be moved by dielectrophoresis and electrorotation simultaneously, with the force and torque having values proportional to the values of the real and imaginary parts of the *Clausius-Mossoti* factor, respectively.

### 2.1.3 Trapping and manipulation of micron-sized objects by DEP

M. Washizu is one of the pioneers who used the dielectrophoresis force to manipulate cells. In two papers appearing in 1989 and 1990 [20, 21], M. Washizu and his co-workers use photolithography for fabricating micro electrodes in order to use dielectrophoresis to control the position of living cells. They also developed what they called “fluidic integrated circuit,” which currently would go by the term “lab-on-a-chip.” They used photolithography and a molding process with silicone to make micro-fluidic channels capable of handling individual cells, and they made a cell-sorter based on dielectrophoresis: cell entering through one micro-fabricated inlet could be deflected electronically into one of the two micro-fabricated outlets.

The polarizability of a cell is a complicated function of its membranes and inner workings, and generally depends on frequency. By exploiting the difference in the frequency-dependent dielectric properties of different cells, it is possible to separate many different kinds of cells from one another and from other micro-organisms in solution. Cells can undergo both positive and negative dielectrophoresis as was shown in [22]. The separation of viable versus nonviable cells was studied carefully with micro-fabricated electrodes in [23, 24]. Different species of bacteria were separated by using a conductivity gradient [25]. Electrorotation is used to separate leukemia cells from normal blood cells [26].

Field flow fractionation (FFF) is very general chromatographic separation technique in chemistry and biology. The principle of dielectrophoretic field flow fractionation (DEP FFF) is shown schematically in Figure 2-3. The latex beads are levitated when an ac voltage is applied to the electrodes. The levitation height is a function of the dielectric properties of the object being levitated. If these electrodes are introduced into a laminar flow chamber, the flow velocity parallel to the chamber walls is also a function of the height. Thus, the speed at which a object is swept through the chamber depends on the height at which it is levitated, which in turn is a function of its dielectric properties, each takes a different time to traverse the chamber. This dependence can be used to separate different objects or cells. In 1994, M. Washizu and co-workers constructed a DEP FFF apparatus and used it to trap DNA of various size and the protein avidin [27], but separation experiments were not reported. Initial experimental demonstration of DEP FFF separation was reported in 1997

where viable and nonviable yeast cells were separated [28]; human leukemia cells were separated from peripheral blood mononuclear cells [29]; and the human breast cancer cells were separated from CD34+ stem cells [30].

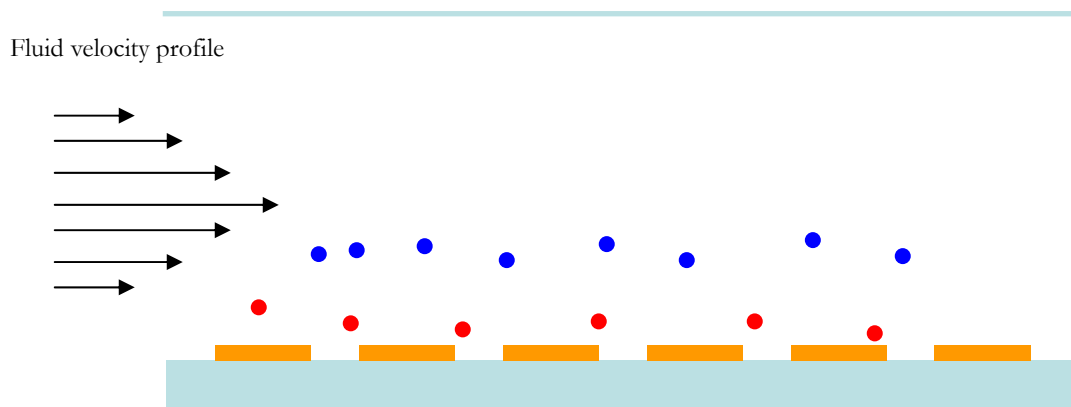


Figure 2-3 Schematic depiction of dielectrophoretic field flow fractionation

Once the electrodes are in place for the dielectrophoretic manipulation of cells, it is straightforward to integrate further optical and electrical measurements that are complementary to DEP techniques into the same measurement platform. These can include optical and electrical methods of genetic expression profiling using micro-arrays, with applications in point-of-care clinical diagnostics, biological detection, and many others. J. Cheng and co-workers separated *E. coli* bacteria from a mixture containing human blood cells and integrated this with cell lysing and DNA hybridization analysis on a single chip [31]. DEP was used to separate certain cell types from complex cell populations, which significantly improved the accuracy of gene expression profiling in [32]. In the spirit of integration, an integrated system using DEP, DNA amplification, and electronic DNA hybridization for the detection of *E. coli* and other biological agents was recently developed [33].

#### 2.1.4 Trapping and manipulation of nano-sized objects by DEP

DEP has been successfully applied as a viable technique to manipulate micro-sized objects

such as cells and latex beads. The principle should also be applicable at the nano scale, and it should be in principle possible to manipulate objects such as DNA, proteins, viruses, nanoparticles, nanowires, nanotubes, quantum dots, and possibly even small molecules.

Latex beads have been used extensively in order to test various aspects of dielectrophoresis because they are robust and can be fluorescently labeled, and hence imaged. G. Fuhr and co-workers realized the trapping of aggregates of 14-nm latex beads, aggregates of viruses of diameter around 100 nm, as well as single latex beads down to 650 nm in size [34]. Subsequently H. Morgan achieved trapping of single 93- nm latex beads in [35, 36]. In 1999, M. P. Hughes and H. Morgan separated unlabeled and protein-labeled 216-nm latex beads [37]. The use of latex beads has been and continues to be a good test bed for the use in manipulating micro/nano objects.

In 1990, M. Washizu and co-workers observed the electrostatic orientation and dielectrophoresis of DNA under a high-intensity field produced in a micro-fabricated electrode system, using the fluorescent method as a visualization technique. The stretch and shrink of an individual molecule is observed as the field is switched on and off. They also showed that it is possible to attach DNA to electrodes. Once attached to the electrode, it is bound chemically and remains after the electric field is off [38]. Later they described several possible applications of this technique. They described an optical/DEP technique to sort DNA molecules by size, measured the activity rate of exonuclease digestion of DNA by measuring the double strand length as a function of time, and developed a method to stretch DNA molecules and position them at two different electrodes [39]. The DNA so immobilized is shown to still be biochemically active [40]. This technique was used to study the DNA interaction with other proteins (*Pseudomonas puuda* CamR) in 1999 [41]. M. Washizu and co-workers also measured the polarization of the fluorescent emission light from dielectrophoretically stretched DNA. The polarization of the emitted light was quantitatively measured and correlated with the applied electric field intensity, as well as the pH of the solution [42]. In 2000, M. Washizu used dielectrophoresis to attach both ends of DNA molecules. Optical tweezers are used to manipulate 1- $\mu\text{m}$  latex spheres labeled chemically with the digestive restriction enzyme which cut DNA at certain specific base sequence. This technique is expected to realize space-resolved molecular surgical operations [43].

C. L. Asbury and van den Engh also reported the DNA trapping in 1998 [44]. Asbury used much lower frequency voltages than M. Washizu, and found no stretching of DNA at these frequencies. Furthermore, C. L. Asbury found that DNA did not get attached to the electrodes, in contrast to M. Washizu's experiment. In 2002, C. L. Asbury continued his work by integrating it with a simple micro-fluidic device (PDMS channel) on top of the electrodes [45]. D. Porath used dielectrophoresis to trap 10-nm-long double strands of DNA between Pt electrodes, concluded that the trapped object was DNA and that its electrical properties were semiconducting [46]. Many other researchers up to and since then have considered the electronic properties of DNA as a molecular wire [47].

In 1994, M. Washizu and co-workers studied the effect of dielectrophoresis on the proteins including avidin, concanavalin, chymotrypsinogen and ribonuclease A. These proteins have diameter from 1 to 5 nm. Fluorescence was used to observe the position of the proteins [48]. In a more recent work, M. Washizu and co-workers developed a biosensor for the protein AFP (alpha-fetoprotein), an important diagnostic protein, which is detected in the serum of a liver-cancer patient. They used the DEP properties of proteins as well as 150-nm latex beads with antibodies immobilized on the surface [49]. M. Washizu also showed that ac electric fields could transform a certain protein, the flagellum of a bacteria from one conformation state to another and this process is reproducible and reversible [50]. By electronically controlling the conformational state of proteins, it may be possible to electronically control their biological functions, or even to engineer new functionality into existing or tailor-designed proteins.

G. Fuhr first reported the trapping of viruses in 1996. They used three-dimensional traps to trap fluorescently labeled influenza viruses using negative dielectrophoresis [51]. In later work, H. Morgan used inter-digitated electrode fingers to manipulate the rod-shaped tobacco mosaic viruses [52]. In 1998, M. P. Hughes trapped the Herpes simplex viruses, which are spherical with diameter about 250 nm [53]. Experiment of separating the Herpes simplex viruses from tobacco mosaic viruses was also realized according to their different frequency response to dielectrophoresis [54].

Carbon nanotube, which is expected to be the building blocks for the next generation nanoscale electronic circuits, can also be manipulated by dielectrophoresis. The first dielectrophoretic

manipulation of nanotube ropes was done using dielectrophoresis in 1997 by A. Bezryadin and C. Dekker [55]. A. Bezryadin used cyclonhexane as the solvent, and a dc voltage of 4.5 V between AuPd electrodes spaced by 150 nm. He simultaneously measured the dc current flowing between the electrodes, and was able to see an electric current as soon as nanotube rope was trapped. In 1998, K. Yamamoto and co-workers aligned and attracted the multiwalled nanotubes (MWNTs) of length between 1 and 5  $\mu\text{m}$ , and diameter 5-20 nm to Al electrodes with 400- $\mu\text{m}$  gaps [56]. In 2001, X. Q. Chen carried out a similar study on single-wall nanotubes (SWNTs) dispersed in ethanol [57]. One of the most important issues which prevent the realization of carbon nanotube based circuitry today is the separation of metallic from semiconducting SWNTs either by selective production or by after-growth separation schemes. M. Dimaki and co-workers presented a numerical study of carbon nanotubes subjected to dielectrophoresis, drag force and Brownian motion induced by application of an ac voltage to microelectrodes in a micro-liquid channel. The simulation results suggests that relatively low frequencies, where both semiconducting and metallic nanotubes are subject to positive dielectrophoresis, may be optimal for separation, due to large differences in the magnitude of the dielectrophoresis force [58]. R. Krupke first realized the experiment to separate metallic from semiconducting SWNTs by taking advantage of the difference of the relative dielectric constants. Metallic tubes attracted toward a microelectrode array, leaving semiconducting tubes in the solvent. Proof of the effectiveness of separation is given by a comparative Raman spectroscopy [59]. R. Krupke also used the ac dielectrophoresis for the simultaneous and site-selective deposition of single bundles of SWNTs onto a large number of contacts. With high-voltage pulses, metallic bundles are transformed into Schottky-barrier-type field-effect transistors with p-type, antipolar, or n-type behavior [5]. M. R. Diehl and co-workers have taken this process one step further, and fabricated cross-bar structures by first aligning and immobilizing SWNT bundles in one direction and then in the perpendicular direction. This represents an initial step toward one of the ultimate goals of self-assembled systems and nanotechnology in general: non-lithographic, economical, massively parallel manufacturing of electronic circuits on the nanoscale [60]. Recently, L. Dong and co-workers achieved alignment of an individual semiconducting or metallic SWNT between two electrical contacts. The measurements for this nanotube transistor displayed an on-off ratio and transconductance which is similar to

the ordinary one [6]. In 2001, X. Duan and co-workers used dielectrophoresis to align and electrically contact InP nanowires. By selectively energizing different pairs of electrodes, X. Duan was able to align InP nanowires into a cross-bar topology using layer-by-layer application of dielectrophoresis [61].

### **2.1.5 Disadvantages of micro-electrode based DEP system**

The use of dielectrophoresis has already found numerous applications in biotechnology, nanotechnology and bio-nanotechnology. Using electrodes fabricated by micro/nano fabrication technology, it has been possible to manipulate, trap, separate, and transport DNA, proteins, viruses, cells of various types, metal nanoparticles, latex beads, carbon nanotubes, semiconducting and metallic nanowires and quantum dots.

However, a major disadvantage of this kind of system is that it requires ac power (often with very high frequency) as the input which limits the miniaturization of the device. Furthermore, the fabrication of the micro-electrode system takes substantial effort. It's also difficult to predict the electric field distribution for the micro-electrode system except for the simplest configuration such as the interdigitated electrode geometry, which provides the uncertainty and difficulty for the designers. For the micro-electrodes based dielectrophoresis, usually the micro/nano objects can only be trapped at the edge of the electrodes (positive dielectrophoresis) or the center of the electrodes system (negative dielectrophoresis). Thus the location of the exerted DEP force can not be defined conveniently and the trapped object can not be moved freely. Certain sophisticated electrode geometry can make the moving of objects possible through creating a traveling wave electric field. But it is rather involved to design and fabricate such kind of electrodes system. Another concern about the dielectrophoresis based on micro-electrodes comes from Joule heating due to current flow through the solution. This is especially a question in solutions of biological significance with ionic concentrations that can also carry current. The heating may cause convective fluidic currents which will overcome the dielectrophoretic forces. The amount of Joule heating is difficult to predict, since the conductive properties of the solution at different frequencies may not be known.

## 2.2 Optical tweezers

Optical tweezers make use forces through radiation pressure which arises from the momentum of the light itself. With lasers, one can make these forces large enough to accelerate, decelerate, deflect, guide, and even stably trap small particles. This is a direct consequence of the high intensities and high intensity gradients achievable with coherent light beams. Laser manipulation techniques apply to particles as diverse as atoms, large molecules, small dielectric spheres in the size range of tens of nanometers to tens of micrometers, and even to biological particles such as viruses, single living cells, and organelles within cells. Using of optical tweezers gives a remarkable degree of control over the dynamics of small particles, and is having a major impact in many of the fields in which small particles play a role.

### 2.2.1 Overview of optical tweezers

Optical tweezers were first introduced by scientists at AT&T Bell Laboratories [62]. Optical tweezers use forces exerted by a strongly focused beam of light to trap small objects. Although the theory behind optical tweezers is still being developed, the basic principles are straightforward for objects either much smaller than the wavelength of light or much larger. Small objects develop an electric dipole moment in response to the light's electric field, which is drawn up/down intensity gradients in the electric field toward the focus (similar mechanism as dielectrophoresis). Larger objects act as lenses, refracting the rays of light and redirecting the momentum of their photons, which is shown in Fig. 2-4.

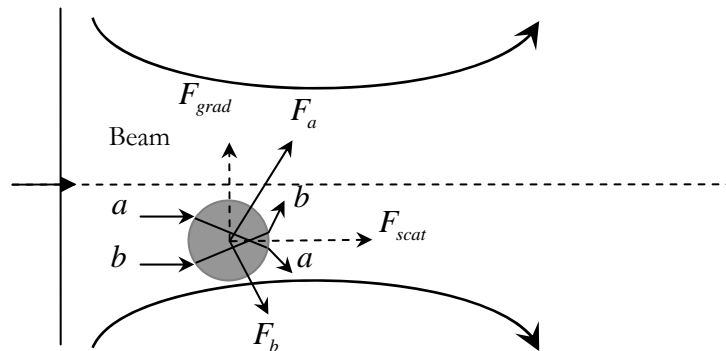


Figure 2-4 Origin of the scattering and gradient force for optical tweezers

Imagine a high index of refraction sphere, many wavelengths in diameter, placed off-axis in a focused Gaussian beam. Consider a typical pair of rays “a” and “b” striking the sphere symmetrically about its center O. Neglecting relatively minor surface reflections, most of the rays refract through the particle, giving rise to forces  $F_a$  and  $F_b$  in the direction of the momentum change. Because the intensity of ray “a” is higher than that of ray “b”, the force  $F_a$  is greater than  $F_b$ . Adding all such symmetrical parts of rays striking the sphere, one sees that the net force can be resolved into two components,  $F_{scat}$ , called the scattering force component pointing in the direction of the incident light, and  $F_{grad}$  a gradient component arising from the gradient in light intensity and point transversely to the high intensity region of the beam. For a particle on axis or in a plane wave,  $F_a = F_b$ , and there is no net gradient force component. For a low index particle placed off-axis, the refraction through the particle reverses,  $F_a < F_b$ , and such a particle should be pushed out of the beam.

## 2.2.2 Trapping and manipulation by optical tweezers

Using optical tweezers, it is now possible to remotely apply controlled force on living cells, internal parts of cells, and large biological molecules. This has resulted in many unique applications.

An early application of tweezers in biology involved the measurement of the torsional compliance of bacterial flagella by twisting a bacterium about a tethered flagellum, calibrating the trapping force against the drag, and measuring the twist sustained by the force [63]. One of the most important biological applications of optical tweezers is in the study of molecular motors. These enzymes interact with the microtubules or actin filaments of the cell to generate the mechanical forces responsible for cell motility, muscle action, cell locomotion, and organelle movement within cells. K. Svoboda and S. M. Block attached single kinesin motor molecules to spheres and placed them directly onto microtubules where they could be activated by ATP [64]. Utilizing this “handle technique”, A. Ashkin and co-workers estimated the force generated by a single motor which is driving a single organelle along microtubules *in vivo* by adopting a useful model system, the giant amoeba *Reticulomyxa* [65]. S. C. Kuo and M. P. Sheetz estimated the force generated by a single kinesin molecule using the biotinylated microtubules and special streptavidin-coated latex

microspheres as handles *in vitro* [66]. An important finding in the field was the study of the detailed motion of a single kinesin molecule into a sequence of 8-nm steps as it advanced along a microtubule by optical trapping interferometry [67]. Afterward, K. Svoboda and S. M. Block measured the complete force–velocity curve of single kinesin motors attached to silica beads as a function of ATP concentrations [68]. A recent exciting advance in the field was the extension of tweezers force measuring techniques to a new class of motors, nucleic acid motor enzymes. The force produced by a single *E. coli* RNA polymerase enzyme was measured optically as it pulled itself along a DNA molecule while synthesizing an RNA transcript. This force is substantially larger than those measured for the cytoskeletal motors kinesin and myosin. The data is consistent with efficient conversion of the energy released by RNA synthesis into mechanical work [69].

Optical tweezers also has been used to examine the mechanical properties of microtubules, actin filaments, and DNA. M. Kurachi et al. measured the flexural rigidity of microtubules by attaching polystyrene beads and bending them with tweezers [70]. Single molecules of double-strand DNA were stretched with force-measuring optical tweezers. When the stress was relaxed below 65 pN, the molecules rapidly contracted to the normal lengths. It is suggested that the overstretched form may play a important role in the energetics of DNA recombination [71]. J. Dai and M. P. Sheetz made the first study of the mechanical properties of membranes on the leading edges of migrating neuronal growth cones by pulling out membrane tethers with tweezers. The force to extend the membrane and the membrane surface viscosity were determined [72].

### **2.2.3 Rotation control by optical tweezers**

Recently, researchers have been working on rotating microparticles and biological particles using optical tweezers, in conjunction with other auxiliary methods or by altering the optical tweezers configuration.

R. C. Gauthier applied the enhanced ray-optics approach to modeling the behavior of the trapping torque of cylindrical micro-objects and the results indicated that the elongated cylindrical objects should align the longest diagonal dimension with the propagation axis of the laser beam, which is consistent with the experimental result [73, 74]. S. Sato and etc. used

the high-order mode Nd : YAG laser beams ( $TEM_{0n}$ ) to realize the rotation of red blood cells. The intensity distribution of the laser beam is not uniform and the resultant trapping force appears to be spatially different. When the laser beam is rotated around the axis, a synchronous rotation of the trapped cell can be observed [75]. E. Higurashi and etc. demonstrated the directional high-speed rotation by radiation pressure for anisotropic micro-objects fabricated by reactive ion-beam etching [76]. Giving the micro-objects an anisotropic geometry produces a torque as a result of the net radiation pressure on their surfaces from a symmetrical input intensity profile. Later A. Yamamoto and etc. adopted the same mechanism to achieve the self-rotation of a particle with anisotropic shape. They also measured the rotation rate from temporal variation of light scattered from the rotating particle. The measured rotation rate seemed to be linearly dependent on the trapping beam power. Furthermore they controlled the rotation rate by a feedback loop connecting the measured rotation rate and the trapping beam power [77].

H. He and H. Rubinsztein-Dunlop observed the transfer of angular momentum of absorptive particles from a laser beam with a phase singularity and the resulting rotation of the particles. With a laser power of a few milliwatts, the rotation speed of the particles lies between 1 and 10 Hz depending on the size and shape of the particle [78]. Later they showed that an optical torque can also be induced on microscopic birefringent particles (calcite crystals) using the typical setup of optical tweezers. Depending on the polarization of the incident beam, the particles either become aligned with the plane of polarization (and thus can be rotated through specific angles) or spin with constant rotation frequency [79]. E. Higurashi and etc. combined micromachine and a processable polymer material having a large birefringence to fabricate the shape-controlled birefringent micro-objects with known location of the optic axis. They experimentally demonstrate angular alignment resulting from the transfer of angular momentum due to the photon spin induced by birefringence to the trapped birefringent micro-object when using linearly polarized light [80]. In 2001, the same group at NTT fabricated microlenses and microprisms by  $O_2$  RIE of a transparent fluorinated polyimide film having in-plane birefringence. Then the fabricated microcomponents were made to align at desired angular position by changing the direction of the polarization plane of the trapping beam. By repeating the alignment on the substrate,

a series of microcomponents can be aligned to form a micro-optical system [81].

A. T. O’Neil and M. J. Padgett proposed a new method of rotational control of objects: inserting a rectangular aperture into the optical beam results in a focused spot that also has rectangular symmetry. They showed that an asymmetric object trapped in the beam has its angular orientation fixed such that rotation of the aperture results in direct rotation of the particle [82].

#### **2.2.4 Disadvantages of optical tweezers**

Optical tweezers have emerged as a powerful tool in molecular and cell biology. However, an undesired drawback of optical trapping has been the damage induced by the intense trapping light. In practice, such damage limits the exposure time for trapped specimens and has proved to be a significant problem for some studies. Indeed, Ashkin first encountered this problem and coined the colorful term “opticutition” to describe the laser-induced death of specimens [83]. The potential for damage is readily appreciated by computing the light level at the diffraction-limited focus of a typical trapping laser: for a power of 100 mW, the intensity is  $10^7$  W/cm<sup>2</sup>, with an associated flux of  $10^{26}$  photons/s•cm<sup>2</sup>. Proposed mechanisms for photodamages include local heating, two photon absorption and photochemical processes leading to creation of reactive chemical species [84].

Those approaches based on optical tweezers which realize the rotation control either can only be applied on certain kind of micro objects (with anisotropic shape or birefringent property) or requires revised optical beam with exquisite optical design. Furthermore, most of them are not able to provide the convenient and precise control of the orientation of micro objects.

### **2.3 Other approaches**

Other approaches including optoelectronic tweezers, magnetic tweezers, hydrodynamic focusing and etc. have also been developed to realize the trapping and rotation of micro/nano objects.

### **2.3.1 Optoelectronic tweezers**

Instead of trapping cells and particles directly using optical force, P. Y. Chiou and M. C. Wu proposed to utilize direct optical images to create high-resolution dielectrophoresis electrode for the parallel manipulation of single particles. A photosensitive device layer forms “virtual electrode” upon exposure to light, creating non-uniformities in an applied electric field which gives rise to the dielectrophoresis force. Since the light is only used to turn on the “virtual electrode” in this approach, it requires much less optical intensity than optical tweezers. However, it lacks the ability to control the orientation of the micro objects [85].

### **2.3.2 Magnetic tweezers**

The early setups able to manipulate magnetic objects in solution were constructed by biophysists for in vivo study of the viscoelastic properties of the cytoplasm. More recently, this technique has been applied to the rheology of actin filament solutions. After the first experiments by Sackman and co-workers, in which the motion of magnetic particles was confined to a single horizontal axis [86], Amblad et al. built a micromanipulator for precise and easily controlled two-dimensional translation and rotation of micrometric beads [87]. C. Gosse et al. described the concept of magnetic tweezers which firstly realized the manipulation at the single-biomolecular level [88]. The apparatus of the magnetic tweezers is very similar to that of optical tweezers. The intensity profile of the trapping beam in optical tweezers corresponds to a real potential well that traps the micro objects in a precise location. In the setup of magnetic tweezers, a system of electromagnets creates field gradients, producing a force on a magnetic probe. The intensity and direction of force can be changed by altering the current running through the coil. The magnetic tweezers show advantages over optical tweezers as they eliminate possible damages to the sample due to localized heating. However, similar to micro-electrode based dielectrophoresis, the location of the magnetic force can not be defined conveniently and the trapped object can not be moved freely.

### **2.3.3 Hydrodynamic focusing**

Hydrodynamic focusing provides another means for positioning small quantities of analytes

with nanoscale precision in two dimensions as well as isolating sample from the channel wall surfaces. The two-dimensional hydrodynamic focusing involves using two outer sheath flows on each side of a central sample flow to laterally constrain the sample flow. This is desirable because it can localize the sample to the center region of the microfluidic channel. Three dimensional hydrodynamic focusing has also been realized by completely surrounding the sample flow by a cylindrical sheath flow that constrains the sample flow to the center of the channel in both the lateral and the vertical dimensions [89]. This technique is effective for the applications such as flow cytometry for cell sorting, cell patterning, molecular detection and other sensitive bio-analytical assay that require microfluidic confinement of samples and molecules. The disadvantages are that it lacks the manipulation flexibility and requires complex microfluidics fabrication.

## Chapter 3 Theoretical Analysis, Modeling and Simulation of the Opto-Plasmonic Tweezers

For the Opto-Plasmonic Tweezers proposed in Figure 1-1, the incident light is focused on a surface of the gold nanostructure. When the wavelength of incident light is at a correct range, localized surface plasmon resonance can be excited, which consists of oscillating dipoles moving resonantly with the incident electromagnetic field. These dipoles radiate and create a patterned scattering field with large gradient that manipulate the micro and nano object through dielectrophoresis. In the first section of this chapter, the interaction between the incident light and gold nanostructures is discussed. In the second section, the distribution of the scattering field is modeled and used to calculate the dielectrophoresis force in various directions on micro and nano objects. Subsequently, we examine the practical situation when the size of the object is comparable to the non-uniformity of the imposed electric field in order to obtain reasonable simulation result of light-induced dielectrophoresis force. The third section investigates the polarization and dielectrophoresis torque for an elliptical object. We find that fine orientation control can be achieved through adjusting the polarization state of the incident light. In the last section of this chapter, we obtain the physical properties of *Listeria monocytogenes* and use it as an example biological cell to simulate the optical manipulation and rotation of the cell.

### 3.1 Surface plasmon resonance

The interaction between light and noble metal has been a topic of fascination, as well as the subject of intensive physical and chemical research for the past hundred years. At certain wavelength, electrons in noble metal will collectively oscillate together which induces the intense extinction (absorption and scattering) of light, a phenomenon called surface plasmon resonance (SPR). Surface plasmon resonance can be divided into two categories: propagating

surface plasmon resonance (conventional SPR) and localized surface plasmon resonance (LSPR) [90].

Propagating surface plasmons are evanescent electromagnetic waves bounded by flat smooth metal-dielectric interfaces and arise from oscillations of the conduction electrons in the metal. The propagating surface plasmon resonance is usually achieved by focusing the light on a glass substrate coated with a thin film of a noble metal. When the wave vector of the incident light matches that of the propagating surface plasmon, the electrons at the surface of the metal film resonate with the incident electromagnetic field. The coupling of the incident light to the surface plasmons results in a loss of energy and therefore a reduction in the intensity of the reflected light. At certain incident angle, the loss of light in the metallic film is greatest and at which the intensity of reflected light reaches a minimum. This is because the amplitude of the wave vector in the plane of the metallic film depends on the angle at which it strikes the interface. The resonance is very sensitive to the local refractive index changes when chemical or biological analyte binds to the metal film. This sensing mechanism has an inherent advantage over other optical biosensor which require label molecule as a transducer for binding event. Furthermore, it can provide the real time measurement on the course of binding and applicable over a broad range of binding affinities. Remarkable progress has been made in the past in the development of conventional SPR based biosensors utilizing the above principle [91].

When surface plasmons are confined on periodic, colloidal, or other nanostructures, localized optical modes are observed. These optical modes lead to highly localized electromagnetic fields outside the particles, which is called the localized surface plasmon resonance (LSPR) [16]. LSPR has one chief advantage over the conventional SPR: LSPR does not require the precise control of the incident angle and ambient temperature, which are necessary for the conventional SPR. LSPR has already been exploited for the construction of various photonic devices (plasmonic devices [14, 92, 93], surface-enhanced spectroscopies [94, 95, 96], optical filters [97, 98]) and biosensors [99, 100, 99]. The proposed Opto-Plasmonic Tweezers also utilizes LSPR since the localized electromagnetic field radiation of the surface plasmons provides us the ideal candidate to manipulate the micro and nano object through dielectrophoresis.

Localized surface plasmons are charge density oscillations confined to metallic nanostructures, which are shown in Figure 3-1. Excitation of localized surface plasmons by an electric field at the resonant wavelength, results in strong light scattering and an enhancement of the local electromagnetic fields. The resonant frequency and amplitude of the extinction peak are characteristic of the material (typically, gold, silver, or platinum) and are highly sensitive to the size, size distribution and shape of the nanostructures, as well as the local environment.

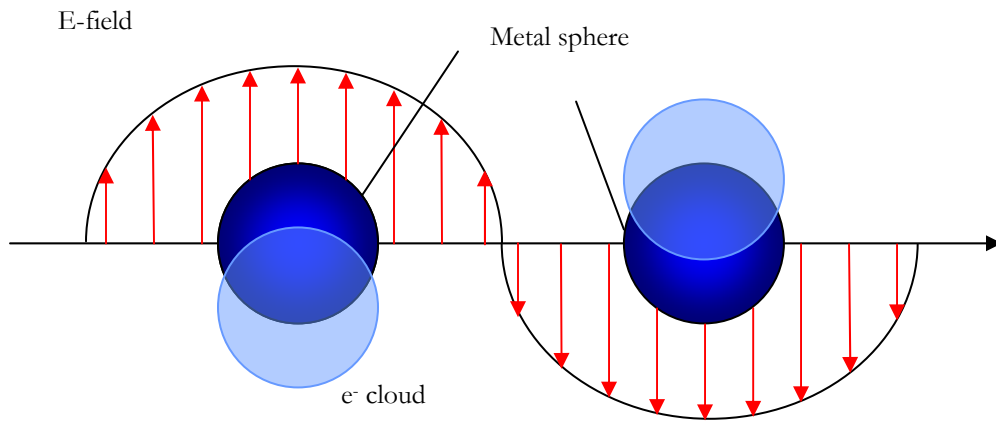


Figure 3-1 Schematics for plasmon oscillation for a sphere, showing the displacement of the conduction electron charge cloud relative to the nuclei.

The simplest theoretical approach available for modeling the optical properties of nanostructures is the classical Mie theory estimation of the extinction of a metallic sphere, the LSPR assumes that the particle and the surrounding medium are homogeneous and can be described by bulk optical dielectric functions. Solving Maxwell's equations lead to a relationship for the extinction cross-section,

$$\sigma_{ext} = \sigma_{abs} + \sigma_{sca} \quad (9)$$

where  $\sigma_{abs}$  and  $\sigma_{sca}$  are the absorption and scattering cross-section respectively. For nanosphere which are significantly smaller than the wavelength of the exciting light ( $\lambda \gg 2R$ , where  $R$  is the radius of the nanosphere), the Mie theory is reduced to [102]:

$$\sigma_{ext}(\omega) = 9 \frac{\omega}{c} V_0 \epsilon_m^{3/2} \left[ \frac{\epsilon_2(\omega)}{(\epsilon_1(\omega) + 2\epsilon_m)^2 + \epsilon_2(\omega)^2} \right] \quad (10)$$

where  $V_o = (4\pi/3)R^3$  is volume of nanoparticles,  $\omega$  is the angular frequency of the exciting radiation,  $\varepsilon_m$  is the dielectric function of the medium surrounding the metallic particles, and  $\varepsilon_1$  and  $\varepsilon_2$  are the real and imaginary part of the dielectric function of the metallic nanoparticles, respectively. As indicated in equation (10), the resonance appears when  $\varepsilon_1(\omega) = -2\varepsilon_m$  if  $\varepsilon_2(\omega)$  is small or if it is weakly dependent on  $\omega$ . The size dependency of the resonance frequency can be accommodated by assuming size-dependent dielectric functions. Equation (10) does not adequately describe the optical behavior of larger ( $2R \geq 30 \text{ nm}$ ) metallic nanoparticles. For such nanoparticles, the extinction cross-section is dominated by higher-order multiple absorption and scattering, and the full Mie equation needs to be used to model the extinction spectra. Mie theory has also been extended to cylindrical nanoparticles. Using discrete dipole approximations optical properties (absorption and scattering efficiencies) have been calculated for metallic nanoparticles having arbitrary shape [103].

Figure 3-2 shows the extinction, scattering and absorption cross section of single Au nanosphere with different diameters ( $D=100 \text{ nm}$ ,  $150 \text{ nm}$ ,  $200 \text{ nm}$ ) which are modeled using the full Mie's equation [104]. As we can see from the plots, when the size of the Au nanosphere increases, the resonance peak becomes broader and moves towards long wavelength region. Meanwhile, the scattering light becomes dominant for large nanospheres.

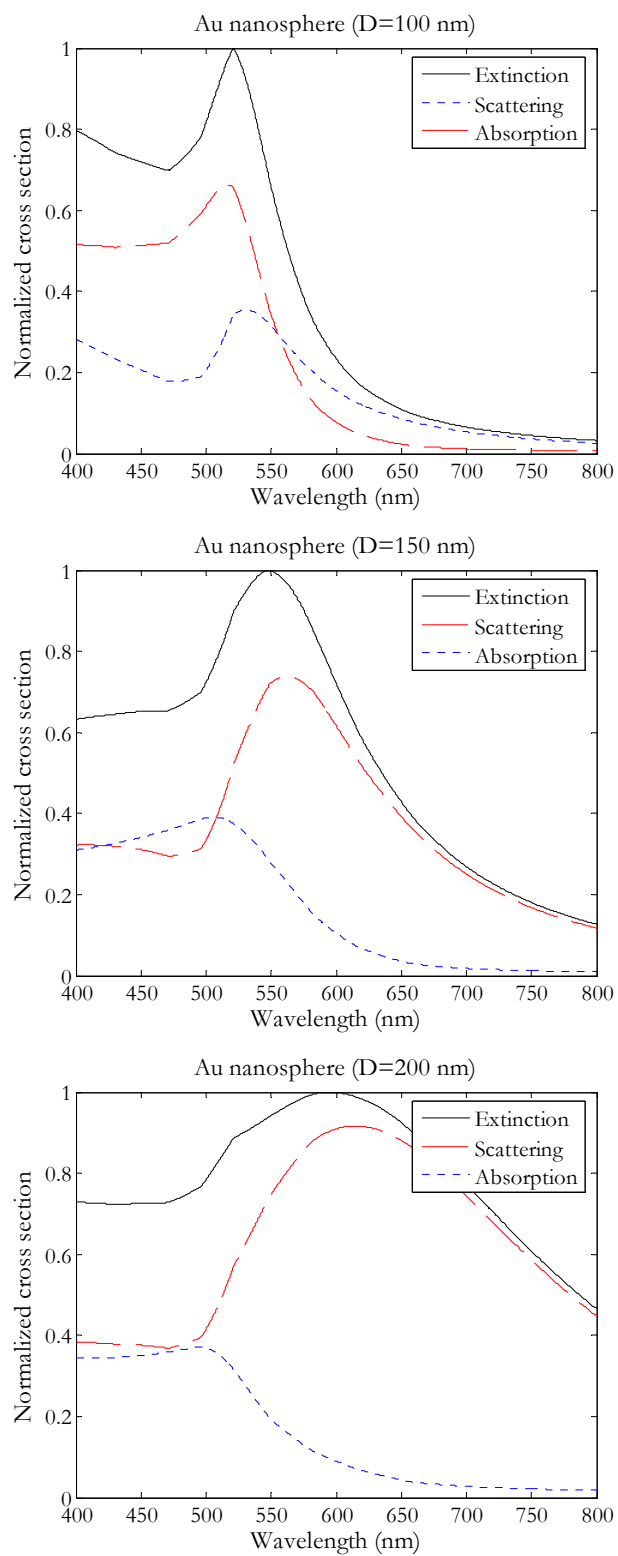


Figure 3-2 Extinction, scattering and absorption cross section of single Au nanosphere with different diameter (D=100 nm, 150 nm, 200 nm).

## 3.2 Light induced dielectrophoresis

The physical principle of the Opto-Plasmonic Tweezers can be described by the diagram shown in Figure 3-3. The theoretical analysis and modeling of each step in Figure 3-3 will be described in the following section.

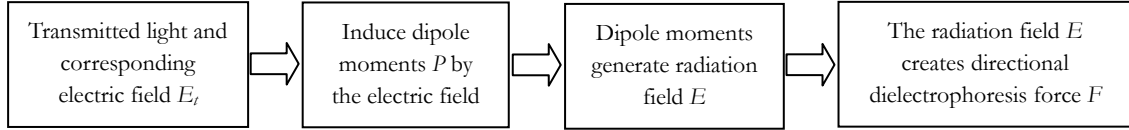


Figure 3-3 Diagram showing the physical principle of the Opto-Plasmonic Tweezers

### 3.2.1 Optical properties of Au

When the light is incident on the Au surface, the corresponding electric field of the incident light induces the free electrons near the Au surface to move resonantly and form oscillating dipole moments. The motion of the free electrons in the electric field can be expressed by the equation

$$m \frac{d^2 \bar{r}}{dt^2} + m\Gamma \frac{d\bar{r}}{dt} = -q\bar{E}_t \quad (10)$$

where  $\Gamma$  represents the damping factor due to electron collision,  $m$  represents the mass of the single electron,  $q$  is the charge of the single electron and  $E_t$  is the transmitted field in Au (see Sec. 3.2.2). Under a monochromatic light excitation,  $\bar{r}$  and  $\bar{E}_t$  have the time dependence  $e^{-j\omega t}$ , and Equation (10) can be simplified as

$$(-\omega^2 m - j\omega m\Gamma)\bar{r}(\omega) = -q\bar{E}_t(\omega) \quad (11)$$

The solution of the differential Equation (11) is given by

$$\bar{r}(\omega) = \frac{q}{m} \cdot \frac{E_t(\omega)}{\omega^2 + i\Gamma\omega} \quad (12)$$

The dipole moment of a single electron is given by

$$\bar{p} = -q\bar{r} = -\frac{q^2}{m} \cdot \frac{\bar{E}_t(\omega)}{\omega^2 + i\Gamma\omega} \quad (13)$$

The dipole moment per unit volume is  $\bar{P} = n\bar{p}$ , where  $n$  is the electron density of the gold. The dielectric susceptibility of the gold is then given by

$$\chi = \frac{P}{\epsilon_0 E_t} = -\frac{nq^2}{\epsilon_0 m} \cdot \frac{1}{\omega^2 + i\Gamma\omega} \quad (14)$$

Assuming  $\chi'(\omega)$  and  $\chi''(\omega)$  are the real and imaginary part of the dielectric susceptibility, the real and imaginary parts of the complex dielectric function are given by

$$\epsilon_r'(\omega) = 1 + \chi'(\omega) = 1 - \frac{\omega_p^2}{\omega^2 + \Gamma^2} \quad (15)$$

$$\epsilon_r''(\omega) = \chi''(\omega) = \omega_p^2 \frac{\Gamma/\omega}{\omega^2 + \Gamma^2} \quad (16)$$

where  $\omega_p$  is defined as the plasma frequency which is given by

$$\omega_p = \sqrt{\frac{nq^2}{\epsilon_0 m}} \quad (17)$$

At optical frequency ( $\omega \gg \Gamma$ ), the complex dielectric function of the gold can be simplified as

$$\epsilon_r'(\omega) = 1 - \frac{\omega_p^2}{\omega^2} \quad (18)$$

$$\epsilon_r''(\omega) = \frac{\omega_p^2 \Gamma}{\omega^3} \quad (19)$$

The complex refractive index of gold is therefore

$$n = \sqrt{\epsilon_r' + j\epsilon_r''} \quad (20)$$

The wave number of the light in gold is given by

$$k = \sqrt{\epsilon_r} k_0 \quad (21)$$

where  $k_0$  is the wave number of light in free space and  $\epsilon_r$  is the complex dielectric function of Au. The wave number  $k$  is also defined as

$$k \equiv \beta + i \frac{1}{2} \alpha \quad (22)$$

where  $\beta$  and  $\alpha$  are the propagation constant and attenuation coefficient of light in gold, respectively. Substituting Equation (18), (19) into Equation (21) and (22), the attenuation coefficient can be calculated

$$\alpha = \sqrt{2} k_0 \times [\sqrt{\varepsilon_r'(\omega)^2 + \varepsilon_r''(\omega)^2} - \varepsilon_r'(\omega)]^{1/2} \quad (23)$$

And the penetration depth of the incident light is given by

$$\delta = \frac{1}{\alpha} = \frac{1}{\sqrt{2} k_0 \times [\sqrt{\varepsilon_r'(\omega)^2 + \varepsilon_r''(\omega)^2} - \varepsilon_r'(\omega)]^{1/2}} \quad (24)$$

Figure 3-4 shows the real part, imaginary part of the dielectric function for gold and penetration depth as a function of light wavelength. As we can see from the plot, the imaginary part of the dielectric function for gold is relatively small compared to the real part at the optical frequency. The penetration depth of the light is on the orders of several nanometers.

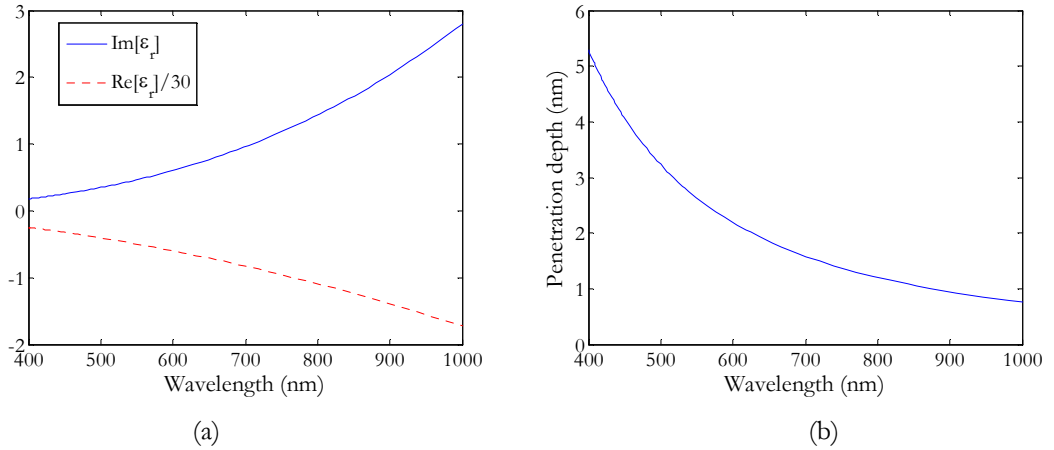


Figure 3-4 (a) Real and imaginary part of the dielectric function; (b) Penetration depth.

### 3.2.2 Light induced dipole momentum

The incident light, with well-defined polarization, has an electric-field component  $\bar{E}_0$ . This electric field oscillates in time with the frequency of the incident light, and has a time dependence of  $e^{-j\omega t}$ . The magnitude of the electric field is related to the intensity of the focused light  $I$  by  $|E_0| = \sqrt{2\eta_1 I}$ , where  $\eta_1$  is the impedance of the liquid solution given by

$$\eta_1 = \frac{\eta_0}{n_1} \quad (25)$$

where  $\eta_0$  is the impedance of free space and  $n_1$  is the refractive index of the liquid solution.

When the incident light incidents normally at the interface between the liquid solution and Au, the transmitted fields in Au follows the form

$$E_t(z) = TE_0 e^{-\frac{\alpha}{2}z} e^{-j\beta z} \quad (26)$$

where  $\alpha$  and  $\beta$  are defined in Equation (22),  $T$  is the transmission coefficient of light from the liquid solution to Au.

The transmission coefficient of light at normal incidence is given by [105]

$$T = \frac{2n_1}{n_1 + n_2} \quad (27)$$

Substituting equation (20) into equation (27),

$$T = \frac{2n_1}{n_1 + \sqrt{\varepsilon_r' + j\varepsilon_r''}} = \frac{2n_1}{n_1 + \sqrt{1 - \frac{\omega_p^2}{\omega^2} + j\frac{\omega_p^2\Gamma}{\omega^3}}} \quad (28)$$

Figure 3-3 suggests that the imaginary part of the dielectric function is much smaller than the real part at the optical frequency. Therefore, equation (28) can be further simplified as

$$T \approx \frac{2n_1}{n_1 + j\sqrt{\frac{\omega_p^2}{\omega^2} - 1}} \quad (29)$$

Substituting equation (29) back into equation (26), the corresponding electric field of light in gold can be written as

$$E_t = \frac{2n_1}{n_1 + j\sqrt{\frac{\omega_p^2}{\omega^2} - 1}} E_0 e^{-\frac{\alpha}{2}z} e^{-j\beta z} \quad (30)$$

Thus the magnitude of the electric field is given by

$$|E_t| = \frac{2n_1}{\sqrt{n_1^2 + \frac{\omega_p^2}{\omega^2} - 1}} E_0 e^{-\frac{\alpha z}{2}} \quad (31)$$

Figure 3-5 shows the transmitted electric field in Au, which decays exponentially in the depth direction of Au.

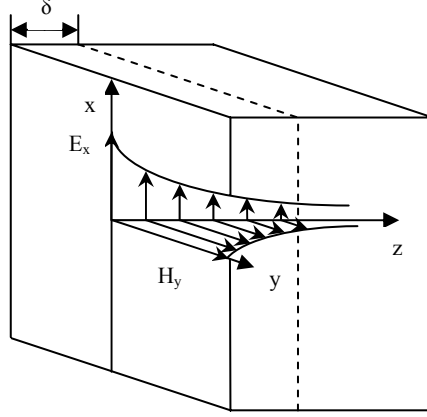


Figure 3-5 Transmitted electric field and magnetic field in Au.

The dipole momentum of a single electron becomes

$$|p| = \left| \frac{q^2 E_t}{m(\omega^2 + i\Gamma\omega)} \right| \approx \frac{q^2 |E_t|}{m\omega^2} = \frac{2q^2 n_1}{m\omega \sqrt{n_1^2 \omega^2 + \omega_p^2 - \omega^2}} E_0 e^{-\frac{\alpha z}{2}} \quad (32)$$

The total dipole momentum can be obtained by performing the following integration

$$|P| = \int_0^h A \cdot n \cdot dp = \int_0^h A \cdot n \cdot \frac{2q^2 n_1}{m\omega \sqrt{n_1^2 \omega^2 + \omega_p^2 - \omega^2}} E_0 e^{-\frac{\alpha z}{2}} dz \quad (33)$$

where  $h$  is the thickness of Au,  $n$  is the free electron density of Au, and  $A$  is the area of light spot. In performing the integration, it is assumed that the light intensity is uniform over area  $A$ . In reality, a Gaussian profile should be taken into consideration. For most cases,  $h$  is much larger than the penetration depth of light in Au, and the total dipole momentum is equal to

$$|P| = \frac{4Anq^2 n_1}{m\omega \alpha \sqrt{n_1^2 \omega^2 + \omega_p^2 - \omega^2}} E_0 = \frac{4Anq^2 n_1}{m\omega \alpha \sqrt{n_1^2 \omega^2 + \omega_p^2 - \omega^2}} \sqrt{2\eta_1 I} \quad (34)$$

### 3.2.3 Scattering field

The resonant dipole moments are known as the Hertzian dipoles, since its magnitude is much smaller than the radiated wavelength of the radiation field. The direction of the Hertzian dipoles is parallel to the electric-field polarization of the light. They radiate the same way as oscillating charges, and create a patterned scattering field. The scattering field forms a half-donut shape, with its axis of evolution aligned with the dipole direction. The field can be described by the following equation at a distance  $r$  and in a direction  $\theta$  from the axis [106]

$$\bar{E} = \frac{k^2 \bar{P}}{4\pi\epsilon_1 r} \sin\theta \exp i\omega(t - r/c) \quad (35)$$

where  $k$  is the wave number, and  $\epsilon_1$  is the dielectric constant of the solution. The variation of the magnitude of the radiated field with  $\theta$  is known as the radiation pattern. Its cross section is shown in Figure 3-6.

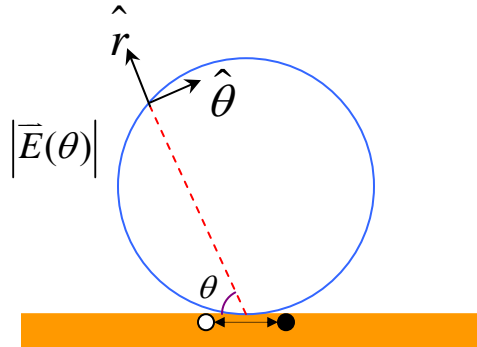


Figure 3-6 Cross-section of the radiation pattern of the electric field generated by the induced dipoles.

### 3.2.4 Force analysis

The highly non-uniform optically induced dipole field shown in the previous section can be utilized to create the DEP force. The DEP force induced by a non-uniform field on a dielectric spherical object is expressed as [107]

$$\bar{F} = 2\pi R^3 \epsilon_1 K^{(1)} \bar{\nabla} |E_{RMS}|^2 \quad (36)$$

where  $R$  is the radius of the spherical object,  $E_{RMS}$  is the root-mean-square (RMS) value of the radiation field, and  $K^{(1)}$  is the *Clausius-Mossotti* factor which is related to the dielectric

constant of the solution  $\epsilon_1$  and the dielectric constant of the object  $\epsilon_2$  by  $K^{(1)} \equiv (\epsilon_2 - \epsilon_1)/(\epsilon_2 + 2\epsilon_1)$ . Equation (36) assumes that the size of the spherical object is much smaller than the non-uniformity of the electric field. Substituting the radiation field obtained above in Equation (35) to Equation (36), the light-induced dielectrophoresis (L-DEP) force at a distance  $r$  and in a direction  $\theta$  from the axis of the dipole becomes:

$$\bar{F}_{L-DEP} = 2\pi R^3 \epsilon_1 K^{(1)} \left( \frac{k^2 P}{4\pi\epsilon_1} \right)^2 \nabla \left( \frac{\sin\theta}{r} \right)^2 \quad (37)$$

which can be expanded as

$$\bar{F}_{L-DEP} = 2\pi R^3 \epsilon_1 K^{(1)} \left( \frac{k^2 P}{4\pi\epsilon_1} \right)^2 \left( -\hat{r} \frac{2}{r^3} \sin^2\theta + \hat{\theta} \frac{2}{r^3} \sin\theta \cos\theta \right) \equiv F_r \hat{r} + F_\theta \hat{\theta} \quad (38)$$

The L-DEP force contains two components: Radial force  $F_r$  in radial direction and angular force  $F_\theta$  in tangential direction. The directions of the two force components are shown in Figure 3-7. The relationship between the radial force and the radial distance at various longitudinal angles is shown in Figure 3-8. And the relationship between the angular force and the longitudinal angle is shown in Figure 3-9. As we can see from the plots, the radial force component represents the trapping effect which pulls the object to the Au surface, and the radial force increases rapidly when the object approaches the Au surface. The direction of the angular force is determined by the sign of  $\sin\theta \cos\theta$ . For  $K^{(1)} > 0$ , which is the case for most of the experimental conditions, the angular force is in the  $+\hat{\theta}$  direction for  $\theta < 90^\circ$ , and the  $-\hat{\theta}$  direction for  $\theta > 90^\circ$ . Therefore, the combination of radial force and angular force pull the particle towards the  $\theta = 90^\circ$  angular force valley, as shown in Figure 3-10. This effect is also indicated in Figure 3-11, which shows the direction of the L-DEP force vector.

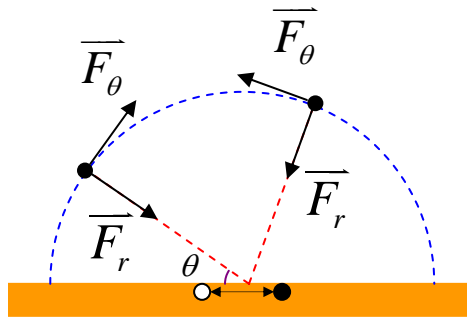


Fig. 3-7 Direction of the two components of the L-DEP force: radial force  $F_r$  in radial direction and angular force  $F_\theta$  in tangential direction.

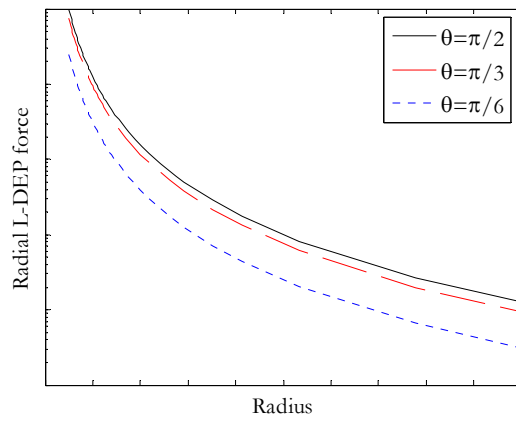


Figure 3-8 Radial L-DEP force versus radial distance at various longitudinal angles.

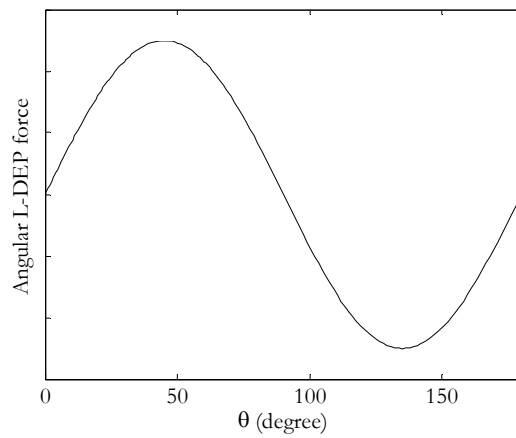


Figure 3-9 Angular L-DEP force versus longitudinal angle

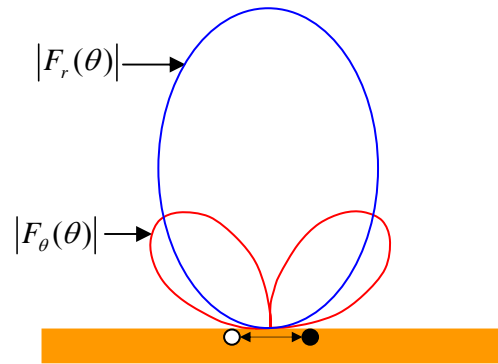


Figure 3-10 Amplitude cross-sections of the radial force and angular force component.

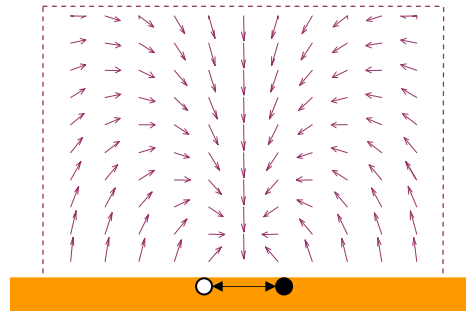


Figure 3-11 Vector plot of the L-DEP force (the length of the vector does not represents its magnitude)

The above force analysis is based on Equation (36), which is derived using the effective moment method. The spherical object is approximated as an induced dipole which is only applicable for the case when the radius of the dielectric sphere is small compared to the length scale of the non-uniformity of the imposed electric field. In the practical situation, to initiate the trapping of the micro/nano objects, the L-DEP force needs to overcome the Brownian motion induced by the thermal energy, which requires that the dimension of the effective trapping region is similar to the radius of the spherical object. Therefore, to get reasonable simulation result, the object needs to be divided into many small spherical elements. After this, the L-DEP force can be calculated for each element and the total L-DEP force exerted on the object can be obtained by adding all the individual force vectors together. For this purpose, a Cartesian coordinate system is built as shown in Figure 3-12.

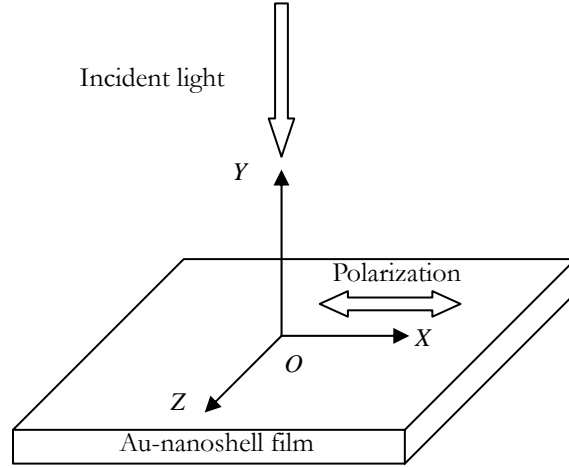
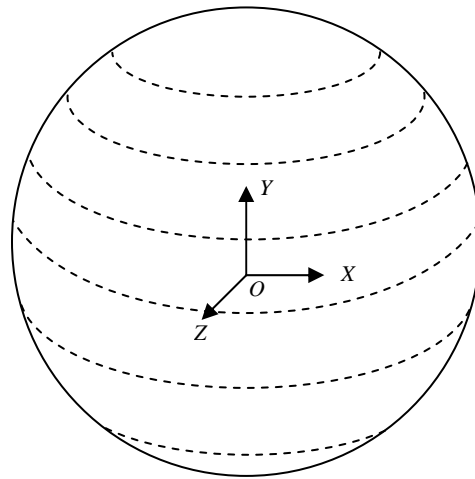


Figure 3-12 Cartesian coordinate for calculating the L-DEP force.

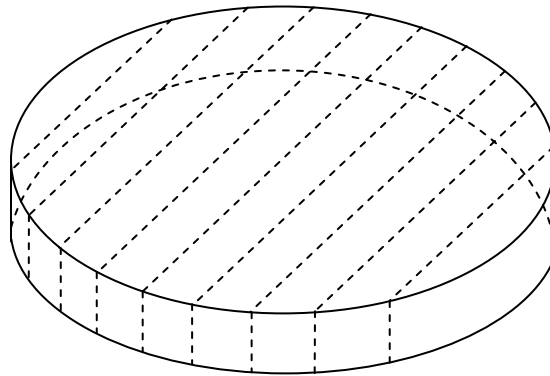
In this new coordinate system, Equation (38) becomes

$$\begin{aligned}
 F_{L-DEP_x} &= 2\pi R^3 \varepsilon_1 K^{(1)} \left( \frac{k^2 P}{4\pi \varepsilon_1} \right)^2 \left( \frac{-2x(y^2 + z^2)}{(x^2 + y^2 + z^2)^3} \right) \\
 F_{L-DEP_y} &= 2\pi R^3 \varepsilon_1 K^{(1)} \left( \frac{k^2 P}{4\pi \varepsilon_1} \right)^2 \left( \frac{-y(y^2 + z^2) + yx^2}{(x^2 + y^2 + z^2)^3} \right) \\
 F_{L-DEP_z} &= 2\pi R^3 \varepsilon_1 K^{(1)} \left( \frac{k^2 P}{4\pi \varepsilon_1} \right)^2 \left( \frac{-z(y^2 + z^2) + zx^2}{(x^2 + y^2 + z^2)^3} \right)
 \end{aligned} \tag{39}$$

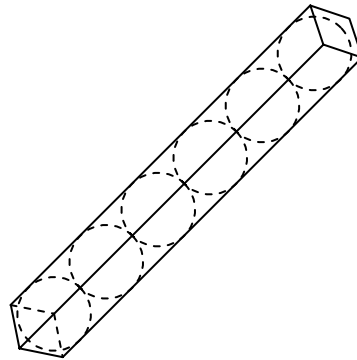
Figure 3-13 shows the procedures to divide the object into finite spherical elements. In (a) the sphere is cut along the plane  $\overline{XOZ}$  and the spacing between the adjacent cutting planes is set as  $h$ . The divided component can be approximated as a cylinder as long as  $h$  is small enough. (b) Each cylinder is cut along the plane  $\overline{YOZ}$  and the spacing between the adjacent cutting planes is the same in (a). The resulting component can be approximated as a rectangle with its width and height equal to  $h$ . (c) Each rectangle can be viewed as a linear array of small spheres with the diameter  $h$ .



(a)



(b)



(c)

Figure 3-13 The procedures to divide the object into spherical elements.

MATLAB is used to carry out the above calculation using the physical constants and input parameters which are listed in table 3-1. Figure 3-14 visualizes the 2D spatial distribution of the L-DEP force in plane  $\overline{XOY}$  and  $\overline{YOZ}$ . The simulation result shows that the L-DEP

force of  $\sim 1 \text{ pN}$  can be achieved at a distance of  $\sim 3 \text{ }\mu\text{m}$ , with incident light intensity as small as  $100 \mu\text{W} / 100 \mu\text{m}^2$ . Such optical intensity is much lower than the requirement for conventional optical tweezers.

Parameters	Symbol	Value
Mass of a single electron	$m$	$9.1 \times 10^{-31} \text{ Kg}$
Charge of a single electron	$q$	$1.6 \times 10^{-19} \text{ C}$
Permittivity in free space	$\epsilon_0$	$8.85 \times 10^{-12} \text{ F / m}$
Permeability in free space	$\mu_0$	$4\pi \times 10^{-7} \text{ H / m}$
Refractive index of the object	$n_o$	2
Refractive index of the medium	$n_m$	1.33
Light velocity in free space	$c$	$3 \times 10^8 \text{ m / s}$
Free electron density of Au	$\delta$	$5.9 \times 10^{28} \text{ / m}^3$
Damping factor of Au	$\Gamma$	$10^{14} \text{ rad / s}$
Area of the light spot	$A$	$100 \mu\text{m}^2$
Wavelength of incident light	$\lambda$	$600 \text{ nm}$
Power of incident light	$P$	$100 \mu\text{W}$

Table 3-1 Physical constants and input parameters used in calculation of L-DEP force

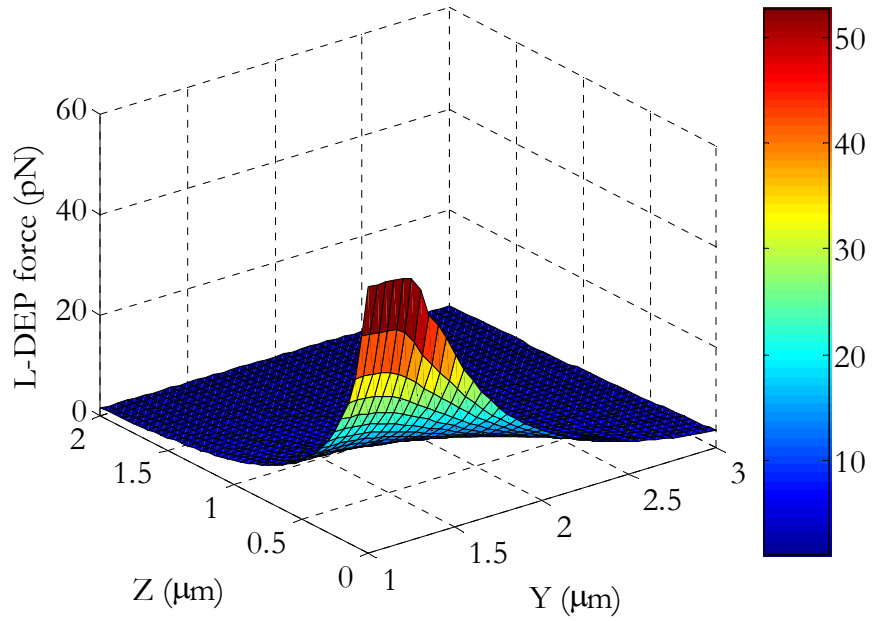
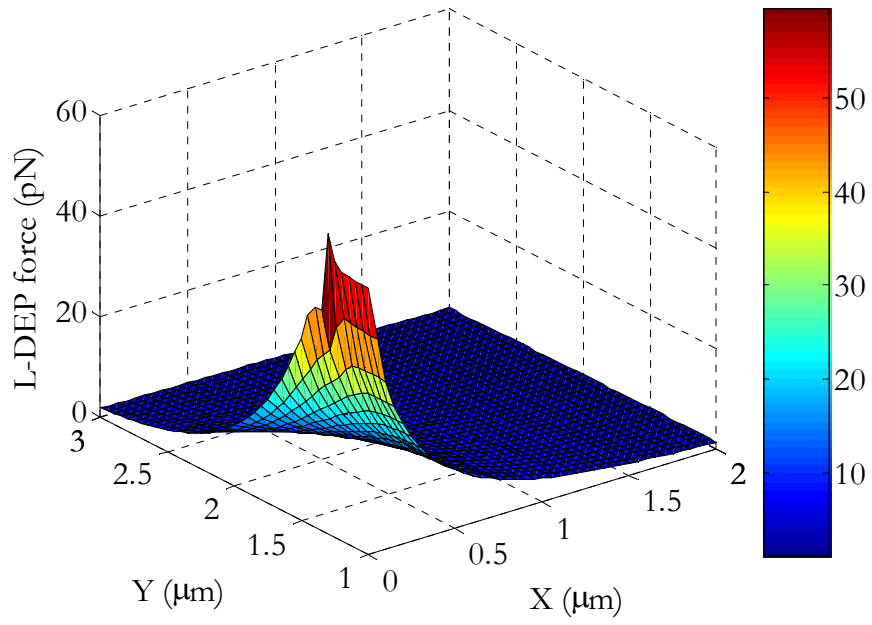


Figure 3-14 2D spatial distribution of the L-DEP force in plane  $\overline{XOY}$  and  $\overline{YOZ}$ .

### 3.2.5 Trapping trajectory

As discussed before, the L-DEP force needs to overcome the Brownian motion, which can be treated as a random force whose maximum value is roughly given by  $F_{thermal} = k_B T / 2R$ , where  $k_B$  is the Boltzmann constant and  $R$  is the radius of the dielectric sphere. For  $R = 1\mu m$ , the equivalent thermal force is about  $0.002 pN$ . For the object moving along the Y axis, the calculation result shows that the L-DEP force can be sufficient to initiate the motion for a dielectric sphere on the Y axis as far as  $34\mu m$  measured from the Au-nanoshell film. For the dielectric sphere within the effective region, it will be trapped to the Au surface as the L-DEP force increases rapidly when the dielectric sphere approaches the Au surface. The Brownian motion can be ignored since the L-DEP force is several orders larger than the equivalent thermal force according to the calculations above. The viscous drag force is related to the immediate velocity of the object by

$$F_{friction} = f \cdot v \quad (40)$$

where  $f$  is the friction factor which is determined by the viscosity of the solution and the geometry of the object. For the sphere with the radius  $a$ , the friction factor is given by

$$f = 2\pi\eta a \quad (41)$$

where  $\eta$  is the viscosity.

Thus the trapping trajectory can be calculated by solving the following ordinary differential equations representing Newton's Law:

$$\begin{cases} F_{L-DEP_x}(x, y, z) - f \cdot \frac{dx}{dt} = m \frac{d^2x}{dt^2} \\ F_{L-DEP_y}(x, y, z) - f \cdot \frac{dy}{dt} = m \frac{d^2y}{dt^2} \\ F_{L-DEP_z}(x, y, z) - f \cdot \frac{dz}{dt} = m \frac{d^2z}{dt^2} \end{cases} \quad (42)$$

Figure 3-13 shows the calculation result of the 3D trapping trajectory, assuming the initiation position of the object is at coordinate  $(10\mu m, 10\mu m, 10\mu m)$ . The result shows that the object will be pulled toward the Au surface and trapped very close to the focused light spot. After this, the trapped object can also be moved freely by adjusting the location of light beam.

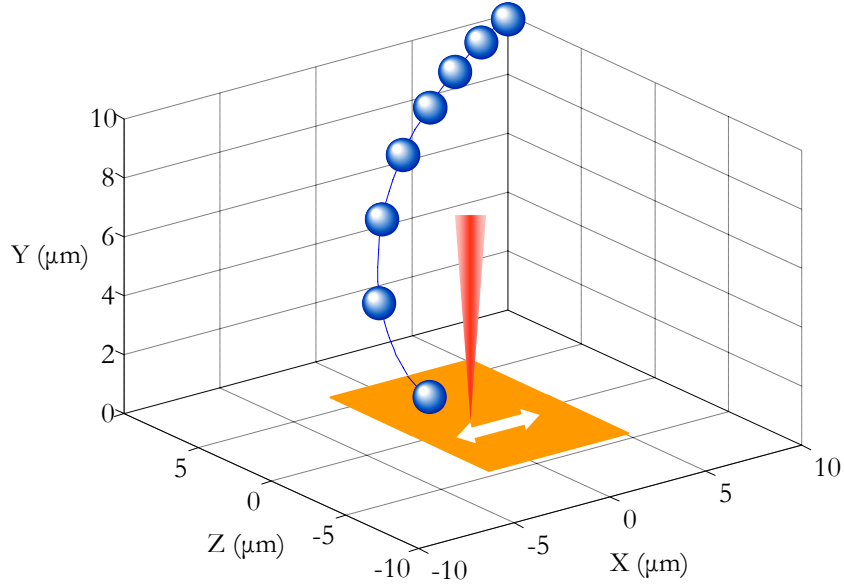


Figure 3-15 Simulated 3D trapping trajectory with equal time interval for the object which is trapped to the surface of the Au-nanoshell film.

### 3.2.6 Orientation control for elliptical object

The analysis in the previous section can be expanded to non-spherical objects. An interesting investigation is to study the steady orientation of an elliptical object under the light-induced dielectrophoresis. Figure 3-16 shows an elliptical object with the long axis  $\overline{AB}$  or  $\overline{A'B'}$  placed above the Au-nanoshell film (using the same Cartesian coordinate system as Figure 3-12). The rotation behavior of the elliptical object can be obtained by dividing the object into many spherical elements and studying the exerted torque on one element. Assuming the coordinate of one element is  $(x_0, y_0, z_0)$ , the L-DEP torque in clockwise direction is given by

$$M = F_z(x_0, y_0, z_0) \cdot x_0 - F_x(x_0, y_0, z_0) \cdot z_0 \quad (43)$$

By substituting the expression of L-DEP force in Cartesian coordinates, equation (43) becomes

$$M = 2\pi R^3 \varepsilon_1 K^{(1)} \left( \frac{k^2 P}{4\pi \varepsilon_1} \right)^2 \frac{x_0 z_0}{(x_0^2 + y_0^2 + z_0^2)^2} \quad (44)$$

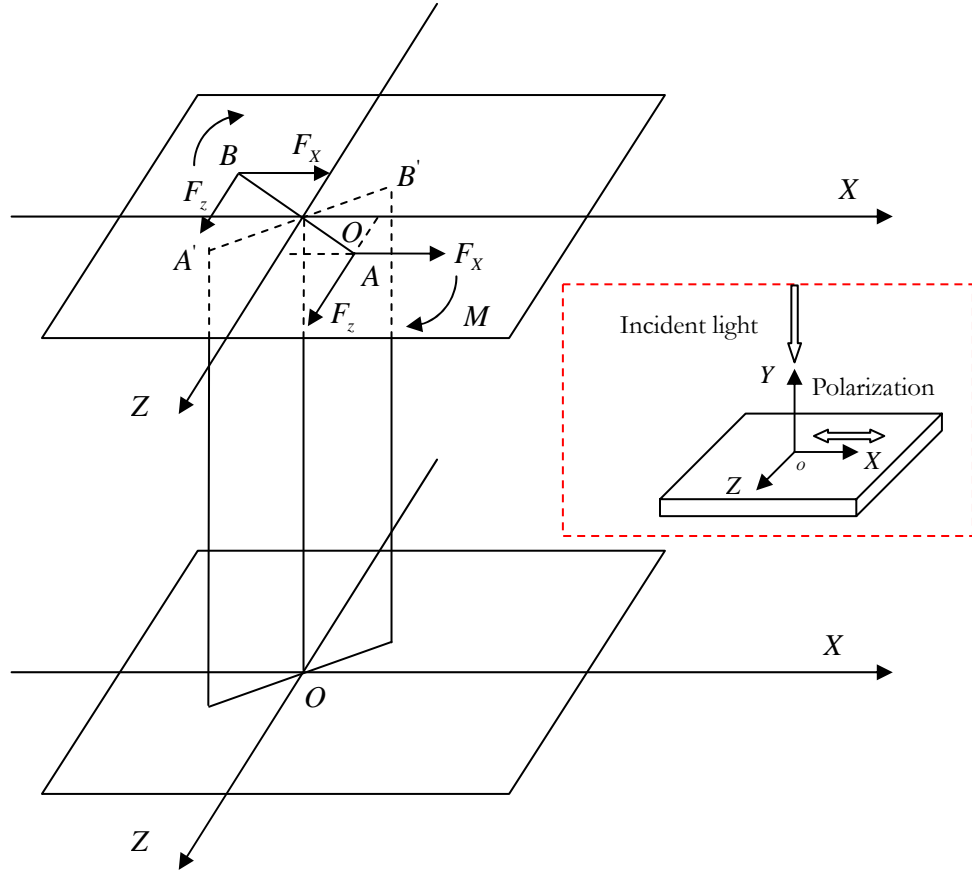


Figure 3-16 Orientation behavior of the elliptical object under light induced dielectrophoresis. The inset is the same as Figure 3-12, which shows the Cartesian coordinate system.

We can see that the L-DEP torques on all elements are clockwise if the long axis of the elliptical object is  $\overline{AB}$  ( $x_0 z_0 > 0$ ,  $M > 0$ ), the L-DEP torques on all elements are counter-clockwise if the long axis of the elliptical object is  $\overline{A'B'}$  ( $x_0 z_0 < 0$ ,  $M < 0$ ). This implies that the long axis of the elliptical object will be aligned to Z axis, which is orthogonal to the polarization direction of the incident light. Any deviation from this orientation will cause the torque to force the elliptical object back to the steady orientation. Since the polarization direction of the incident light can be adjusted very precisely, the steady orientation of the elliptical object can be adjusted accordingly. Thus the Opto-Plasmonic Tweezers can not only be used to trapped micro and nano scale objects, but also provide the fine orientation control capability.

### 3.3 Modeling on biological cells

#### 3.3.1 Physical properties of *L. monocytogenes*

By collaborating with Prof. Suzie Pun from the Bioengineering Department of the University of Washington, we use *Listeria monocytogenes* as a model system for the theoretical simulations of the proposed Opto-Plasmonic Tweezers. *L. monocytogenes* is elliptical in shape. It is an intracellular bacterial pathogen that rapidly invades host cells by hijacking the host cells' actin polymerization machinery for motility [108, 109]. The *L. monocytogenes* ActA protein has been identified as the single protein in *L. monocytogenes* responsible for activating actin polymerization [110, 111]. Actin comet tail formation and resulting particle motion can be initiated and visualized in a cell-free extract system [112]. This system has been used to study the motility of *L. monocytogenes* and synthetic, ActA-coated nanoparticles. [113, 114, 115] The actin-propelled particles move along curved paths, and the curvature of the actin-mediated path has been observed to increase as the ActA-modified particle size decreases [116]. This phenomenon has also been observed in Prof. Pun's laboratory, which is shown in Figure 3-17.

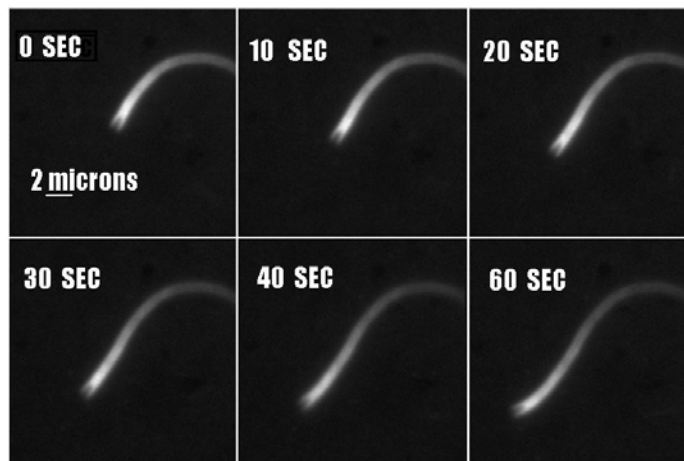


Figure 3-17 Movement of *L. monocytogenes* in cell-free extracts resulting from actin comet tail formation.

[Courtesy of Prof. Suzie Pun]

In order to model the light-induced dielectrophoresis of *L. monocytogenes*, we need to obtain its physical properties such as diameter, length, complex permittivity. *L. monocytogenes* is elliptical in shape and consists of membrane and internal parts which have different

permittivity. For simpler analysis, a spherical particle with the effective diameter  $D$  having a shell with the thickness  $d$  is used to estimate the permittivity of *L. monocytogenes*. This is given by [117]

$$\varepsilon_p^* = \frac{2\varepsilon_m^* + \varepsilon_i^* - 2(\varepsilon_m^* - \varepsilon_i^*)\left(\frac{D}{D+d}\right)^3}{2\varepsilon_m^* + \varepsilon_i^* + (\varepsilon_m^* - \varepsilon_i^*)\left(\frac{D}{D+d}\right)^3} \varepsilon_m^* \quad (45)$$

where  $\varepsilon_m^*$  and  $\varepsilon_i^*$  are the complex permittivity of the membrane and the cell interior, respectively. The effective diameter  $D$  is assumed to equal to  $\sqrt[3]{4R^2l}$ , where  $R$  and  $l$  is the radius and length of *L. monocytogenes*. Table 3-2 gives the parameters used to calculate the equivalent permittivity of *L. monocytogenes*.

Parameter	Symbol	Value
Radius	$R$	$0.4 \mu m$
Length	$l$	$1.3 \mu m$
Membrane thickness	$d$	$10 nm$
Equivalent diameter	$D$	$0.94 \mu m$
Membrane permittivity	$\varepsilon_m$	$6 \times \varepsilon_0$
Membrane conductivity	$\sigma_m$	$10^{-7} S/m$
Cytoplasm permittivity	$\varepsilon_i$	$50 \times \varepsilon_0$
Cytoplasm conductivity	$\sigma_i$	$0.5 S/m$

Table 3-2 Parameters for calculating the equivalent permittivity of *L. monocytogenes*.

Substituting the parameters in Equation 47, the complex permittivity of *L. monocytogenes* can be obtained,

$$\varepsilon_p^* = \frac{(0.531 \times 10^{-10} + \frac{10^{-7}}{j\omega})(0.1298 \times 10^{-8} + \frac{1.4625}{j\omega})}{0.1739 \times 10^{-9} + \frac{0.01875}{j\omega}} (F/m) \quad (46)$$

By substituting the angular frequency corresponding to the incident light wavelength  $\lambda = 600 \text{ nm}$ , the optical permittivity of *L. monocytogenes* is equal to

$$\varepsilon_p^* = 5.31 \times 10^{-11} - 3.5638 \times 10^{-22} j \text{ (F/m)} \quad (47)$$

Notice that the imaginary part is very small compared to the real part and thus can be ignored. The dielectric constant is approximately equal to  $\varepsilon_p / \varepsilon_0 = 6$  and the refractive index is equal to  $n = \sqrt{\varepsilon_r} = 2.4495$ .

### 3.3.2 L-DEP force and the associated torque on *L. monocytogenes*

In this section, *L. monocytogenes* are used as a model system to calculate the L-DEP force and associated torque. The approach in section 3.2.4 is applied here but assuming the object is cylindrical. Figure 3-18 shows the procedure to divide the object into elements. Two Cartesian coordinates systems are set up here:  $O-XYZ$  in which  $X$  axis denotes the polarization direction of incident light, and  $O'-X'Y'Z'$  in which  $Z'$  axis denotes the long axis direction of *L. monocytogenes*. The coordinate conversion relationships between the two coordinate systems are given by,

$$\begin{cases} x' = z \sin \theta + x \cos \theta \\ y' = y \\ z' = z \cos \theta - x \sin \theta \end{cases} \quad (48)$$

Given the center coordinate  $O'$  of *L. monocytogenes* in  $O-XYZ$  coordinate system, the corresponding coordinate in  $O'-X'Y'Z'$  coordinate system can be calculated using Equation (50). After this, the coordinates of all elements of the cylinder in Figure 3-18 can be conveniently expressed in  $O'-X'Y'Z'$  coordinate system according to their relative locations to the center. The next step is to convert the coordinate of each element in  $O'-X'Y'Z'$  coordinate system back into  $O-XYZ$  coordinate system, so that Equation (41) can be utilized to calculate the L-DEP force of each element. Finally all the L-DEP force vectors are added together to get the L-DEP force exerted on the whole cylinder. The input parameters such as light intensity and light spot area are the same as those in Table 3-1. The

simulation results are shown in Figure 3-19 which include the 2D spatial distributions of L-DEP force in  $\overline{XOY}$  ( $z=0$ ) and  $\overline{YOZ}$  ( $x=0$ ). The relationship between L-DEP force and orientation of the long axis is shown in Figure 3-20.

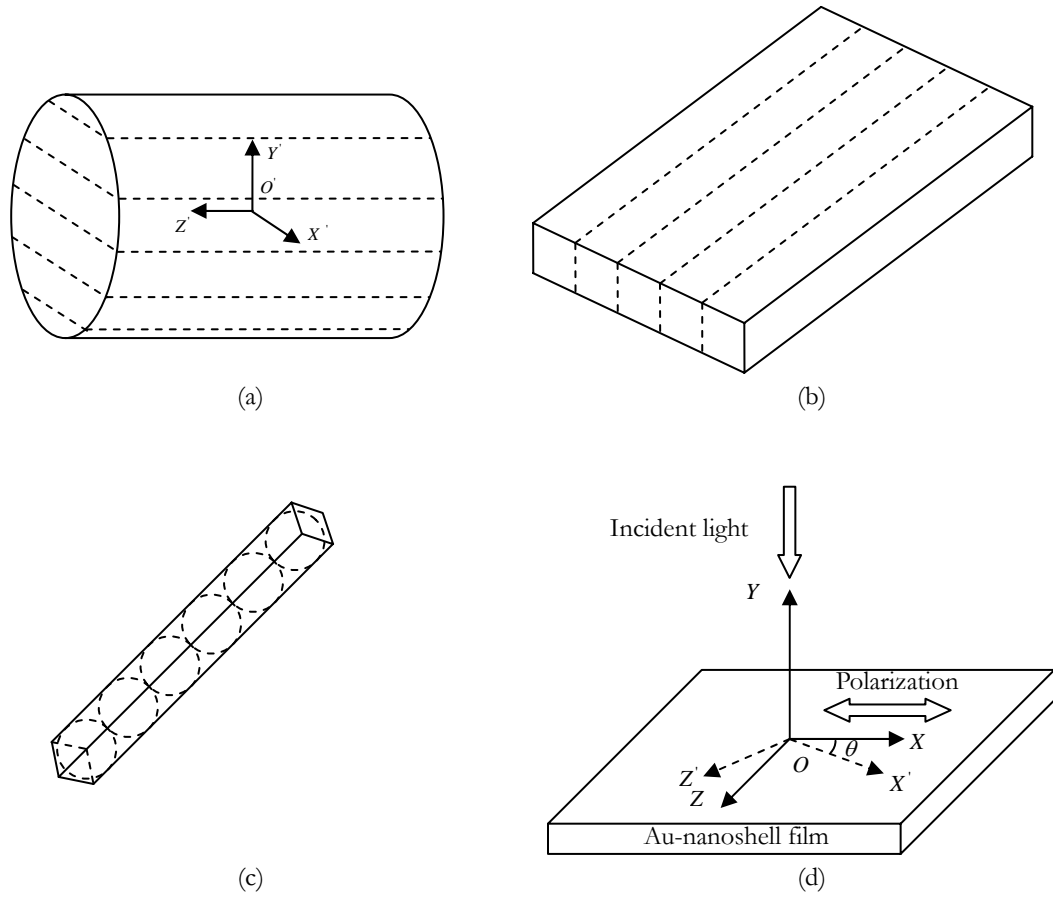
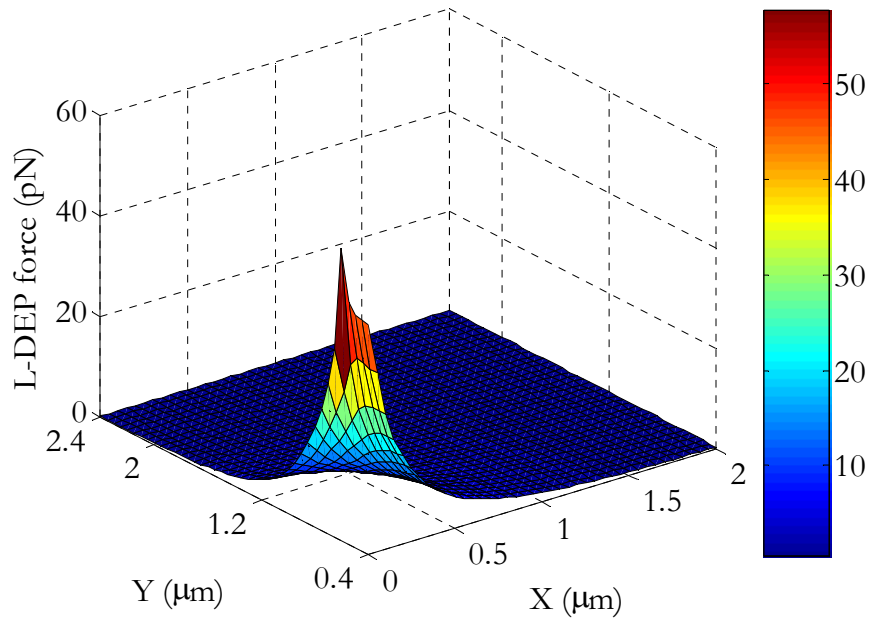
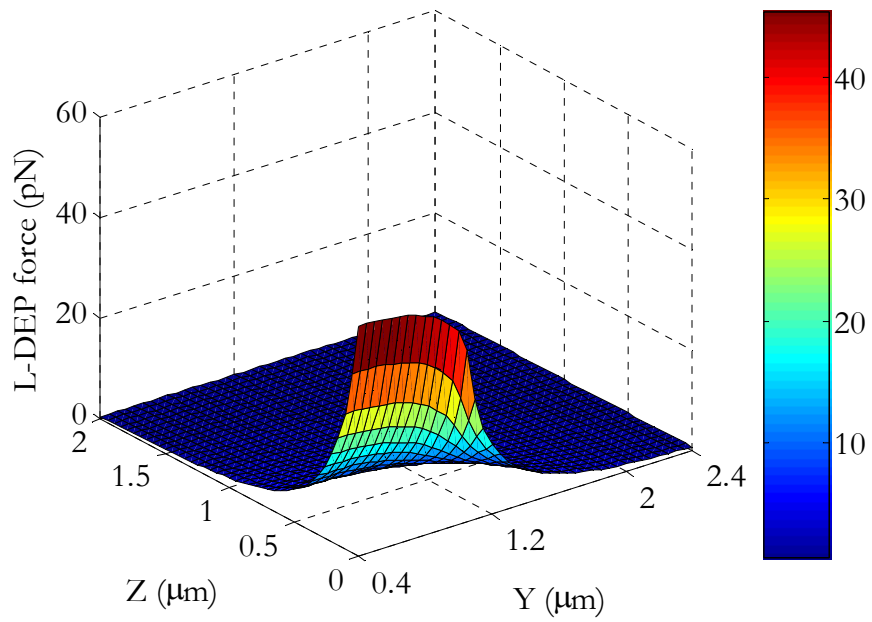


Figure 3-18 (a) (b) (c) The procedures to divide the cylindrical object into spherical elements. (d) Two Cartesian coordinate systems, in which X axis denotes the polarization direction of incident light, Z' axis denotes the long axis direction of *L. monocytogenes*.



(a)



(b)

Figure 3-19 (a) (b) 2D spatial distribution of the L-DEP force on *L. monocytogenes* in plane  $\overline{XOY}$  and  $\overline{YOZ}$ .

Similar to the results in section 3.2.4, the simulation results for *L. monocytogenes* show that the L-DEP force exerted on the cell increase rapidly when the cell approaches the Au-nanoshell film. The L-DEP force of about 1 pN can be achieved at a distance of about 1.8  $\mu\text{m}$ . Figure 3-20 plots the L-DEP force exerted on the cell versus the long axis orientation. We can see that the L-DEP force does not vary significantly when the long axis of the cell has different orientations.

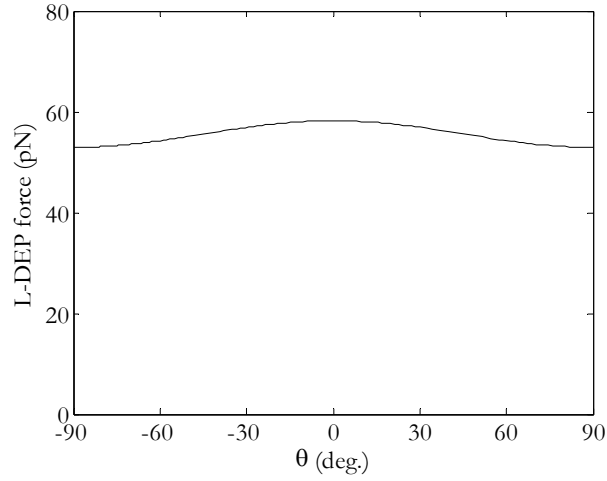


Figure 3-20 L-DEP force on *L. monocytogenes* versus its orientation of the long axis (assuming the center coordinate:  $x = 0, y = 1 \mu\text{m}, z = 0$ )

To study the rotation of long axis of the cell around Y axis, we need to calculate the associated L-DEP torque in  $\overline{XOZ}$  plane. For this purpose, we express the L-DEP force vector of each element in coordinate system  $O-X'Y'Z'$ . As shown in Figure 3-21, the contribution of the torque in counter-clockwise direction is given by,

$$M_p = -F'_x \cdot z' - F'_z \cdot x' \quad (49)$$

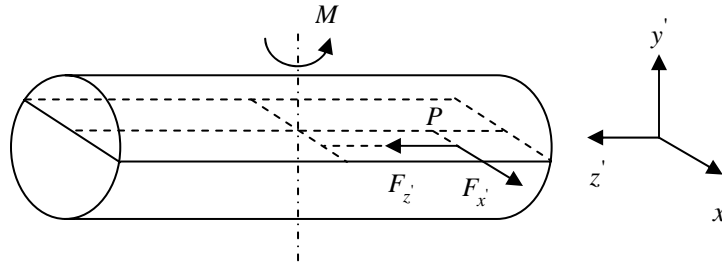


Figure 3-21 Contribution of the torque in  $\overline{XOZ}$  plane of element P

The total exerted L-DEP torque on the cell can be obtained by adding the torques on all the elements. Figure 3-22 shows the total L-DEP torque in  $\overline{XOZ}$  plane as a function of long axis orientation, assuming the center of cell locates at  $(x=0, y=0.4 \mu\text{m}, z=0)$ , which is at the center of light spot and on the surface of Au-nanoshell film.

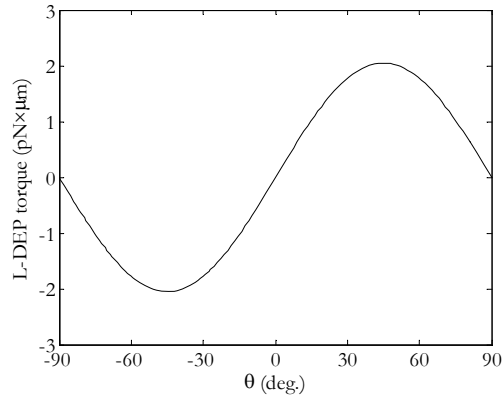


Figure 3-22 The L-DEP torque in  $\overline{XOZ}$  plane on the cell as a function of long axis orientation.

The definition of  $\theta$  is referred to Figure 3-18 (d), which is the angle between  $X$  axis and  $X'$  axis ( $\theta$  is positive in clockwise direction). As we can see from Figure 3-22, the L-DEP torque is positive for  $0^\circ < \theta < 90^\circ$ , which is in counter-clockwise direction; the L-DEP torque is negative for  $-90^\circ < \theta < 0^\circ$ , which is in clockwise direction. The two situations are shown in Figure 3-23. The steady orientation corresponds to  $\theta = 0^\circ$ , when axis  $X$  and  $Z$  coincide with axis  $X'$  and  $Z'$  respectively. This implies that the long axis of the cell will be aligned to orthogonal direction of the polarization direction of the incident light ( $X$  axis denotes the polarization of the incident light,  $Z'$  axis denotes the direction of the long axis of cell).

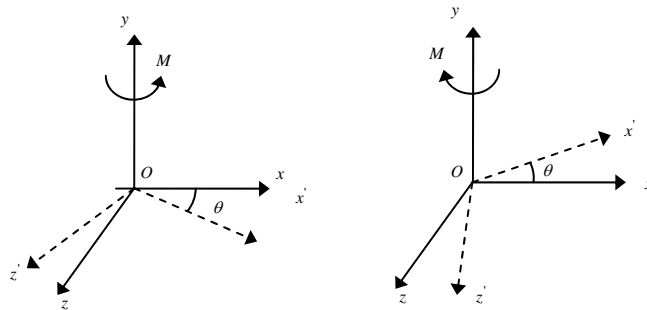


Figure 3-23 L-DEP torque is in counter-clockwise (clockwise) direction when  $\theta$  is positive (negative).

### 3.3.3 Trapping and rotation of *L. monocytogenes*

Following the discussion in section 3.2.5, the trapping trajectory of the cell can be calculated by solving the differential Equations (44). For simplified analysis, we assume the orientation of the long axis of the cell remains the same before the cell arrives at the surface of the Au-nanoshell film since the trapping force does not vary much with different orientations of the long axis. The calculated trapping trajectory is plotted in Figure 3-21.

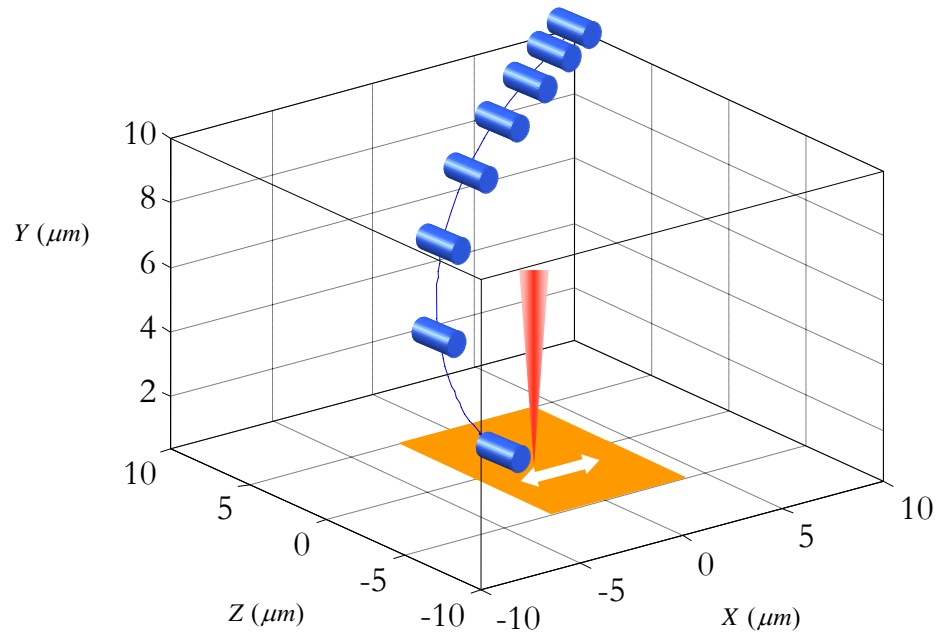


Figure 3-21 Simulated 3D trapping trajectory with equal time interval for the cylindrical cell which is trapped to the surface of the Au-nanoshell film, assuming the orientation of long axis keeps unchanged before arriving at the surface of the Au-nanoshell film.

Similar calculation can be performed to see how the cell aligns its long axis orthogonal to the polarization direction of the incident light, which is shown in Figure 3-22.

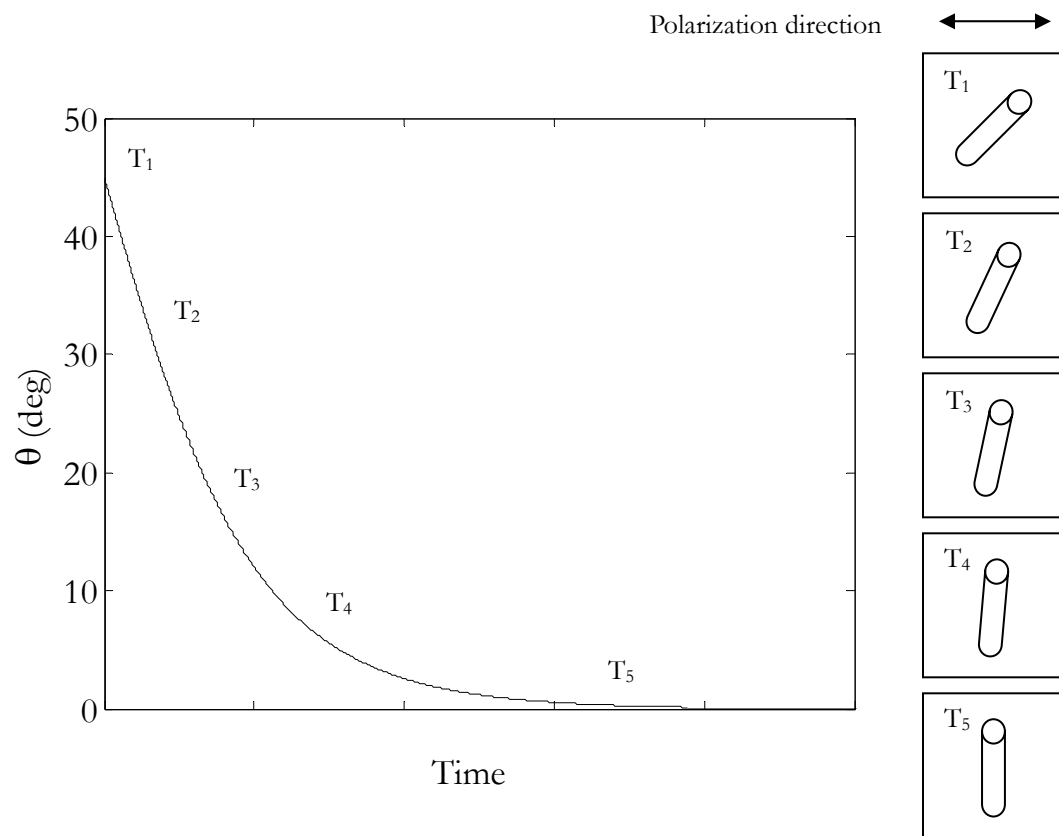


Figure 3-22 The long axis of the cell is aligned orthogonal to the polarization direction of the incident light.

## **Chapter 4 Fabrication and characterization of the Au nanostructure**

The Opto-Plasmonic Tweezers are fundamentally different from the traditional optical tweezers in the underlying physical principles. The Opto-Plasmonic Tweezers make use of the enhanced scattering electric field from Au nanostructures to induce the dielectrophoresis force and torque which are utilized to achieve the trapping and rotation of the micro and nano objects. A bench-top optical system will be built to demonstrate the modeling results discussed in Chapter 3. Figure 4.1 shows the schematic drawing of the experimental system. The polarization of the input light from a laser source is adjusted by a commercial polarization controller. The input light is sent into an optical microscope and directed by a beam-splitter downwards to the sample. The light is focused by the objective lens and forms a small spot on the sample with the Au structures. Micro/nano objects with asymmetrical shapes but well-understood material properties are suspended in an aqueous solution covering the sample. The polarization of the input light is adjusted, and rotation of the particles is observed under the high-power microscope. In addition, the sample sits on a translational stage, therefore trapping and moving of the cells can also be observed when the stage moves relative to the focused light spot.

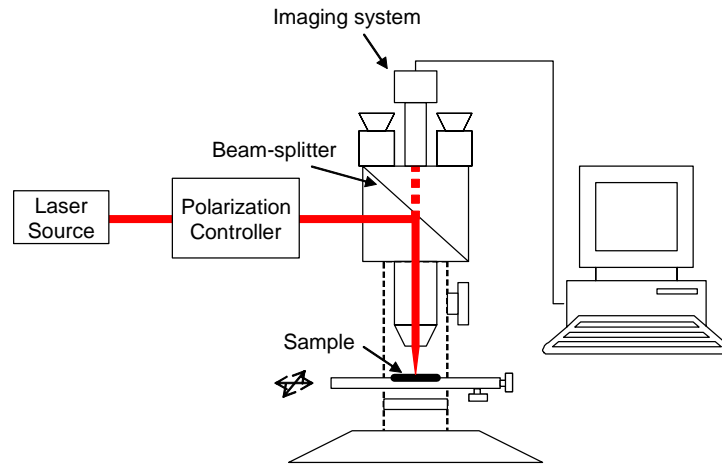


Figure 4-1 Bench-top system for demonstrating optical manipulation with fine orientation control.

The key element of the device is the Au nanostructure which is placed under the aqueous solution in the above setup. Mie theory suggests that the intense scattering field will be excited from the Au nanostructures when the incident photon frequency is resonant with the collective oscillation of the conduction electrons, the localized surface plasmon resonance, discussed in Chapter 3. After the Au nanostructure is made, the scattering peak of the nanostructure will be determined by experiment, and laser with the right wavelength will then be chosen to induce the resonance to demonstrate the trapping and rotation behavior. Thus the first step of this project is to develop a viable construction method of the Au nanostructures. This may also lead to research possibilities for other applications besides the Opto-Plasmonic Tweezers, such as biosensing, plasmonic devices, optical filters, Raman scattering and etc.

E-beam lithography (EBL) is a powerful tool to create nanoscale patterns. But it takes long time to write the patterns, and the cost is expensive. To achieve simple and low-cost fabrication process, we chose chemical self-assembly method to fabricate the Au nanostructure. The approach utilizes the surface-absorbed polystyrene spheres as a template to format the Au nanoshell film [118, 119, 120]. Tools including the scanning electron microscope (SEM), atomic force microscopic (AFM) and conventional optical microscope are used to characterize the nanostructure we made. The analyses of the LSPR spectra of the

samples are also performed using a UV/VIS spectrometers. Further details on fabrication and testing are given as follows.

#### **4.1 Fabrication of Au nanoshell films**

The Au nanoshell film is formatted using surface-adsorbed polystyrene spheres as a template. The use of monodisperse polystyrene spheres covering a wide range of sizes permits the production of equally monodisperse Au nanostructures. The procedure (shown in Fig. 4-2) to build the Au nanoshell film begins with cleaving a small coupon, generally  $1\text{ cm} \times 1\text{ cm}$  area, from a silicon wafer (Ultrasil Corporation, Hayward, CA). The sample is cleaned by rinsing with xylene, acetone, isopropyl alcohol (IPA) and de-ionized (DI) water followed by drying with nitrogen gas. Then, the sample is evaporated with Au in a vacuum of  $5 \times 10^{-6}\text{ Torr}$  at a rate of  $1\text{ \AA}/\text{s}$  to a final thickness of 20 nm using Cr as the adhesion layer. The next step is to prepare the sphere solution 100 mM phosphate buffer ( $\text{pH}=7.6$ ) (Sigma-Aldrich, St. Louis, MO) containing 15 mM carbodiimide solution (1-ethyl-3-(3-(dimethylamino)propyl)carbodiimide, Sigma-Aldrich, St. Louis, MO) and polystyrene suspension (Polysciences, Inc., Warrington, PA or Spherotech, Inc., Libertyville, IL) were mixed and further diluted with deionized water. The sphere suspension is then deposited to the surface of the Au layer. The sphere adsorption begins immediately upon exposure of the substrate to the sphere suspension. To assure consistency in the sample quality, the adsorption process was allowed to continue for about 1 hour. Non-adsorbed spheres are washed away with a copious amount of deionized water; subsequently the formed monolayer of polystyrene sphere is allowed to dry in air. Once dried, the spheres will be firmly adsorbed such that vigorous squirting of water from a wash bottle dislodged very few spheres. At the final step, another 20 nm of Au is evaporated on the sphere monolayer and forms the Au nanoshell film.

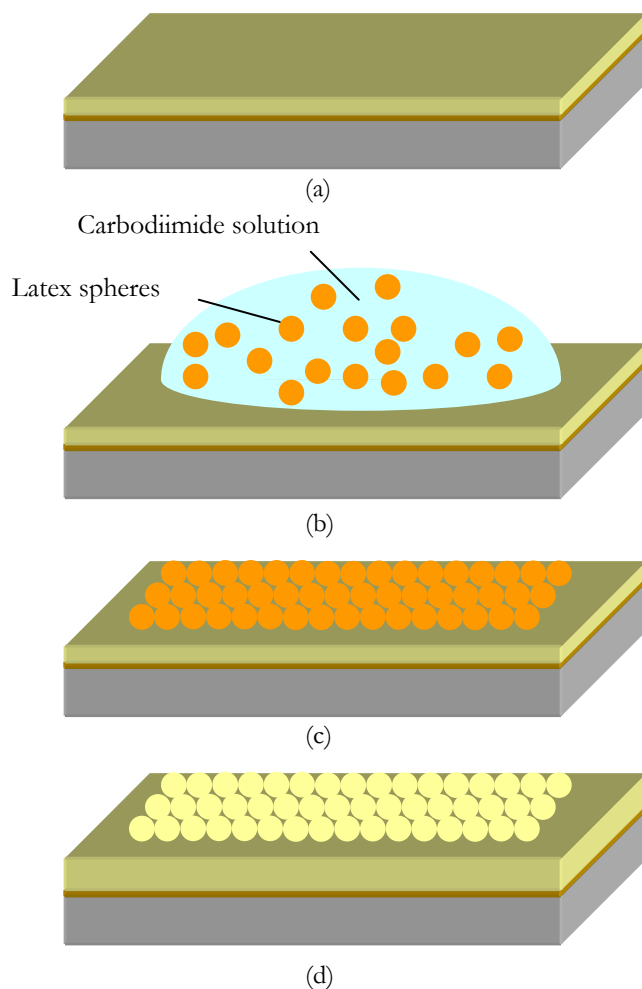


Figure 4-2 Fabrication procedure of cap-shaped Au-nanoshell film: (a) Evaporation of 2 nm Cr and 20 nm Au on the silicon substrate; (b) Exposure to the polystyrene sphere suspension and adsorption of spheres for 1 hour; (c) Removal of non-adsorbed polystyrene spheres and drying of the surface; (d) Evaporation of another layer of Au on top of nanospheres.

#### 4.1.1 Thermal evaporation of Au

For evaporation a thermal evaporator (Auto 306 Vacuum Coating Systems, BOC Edwards Group Inc., Wilmington, MA) was used at a base pressure of  $2 \times 10^{-6}$  Torr; the growth rate was monitored by a quartz crystal microbalance and manually adjusted to 1 Å/s. Gold of 99.95% purity was obtained from. 20 nm of Au were evaporated onto the Si coupon for preparation of Au substrates. The same amount of Au was evaporated onto the adsorbed polystyrene spheres for the final Au nanoshell formation.

#### **4.1.2 Self-assembly of polystyrene spheres**

To prepare the sphere suspension, 100 mM phosphate buffer ( $pH=7.6$ ) containing 15 mM carbodiimide (EDC), polystyrene suspension and deionized water are mixed together at certain ratio in the Eppendorf tube. The sample after Au evaporation is cleaned using oxygen plasma for about 1 minute to remove the organic impurities on the surface. Then the sphere suspension of 25  $\mu\text{l}$  is deposited on the surface of the sample using a pipette. The suspension forms a hemispherical shape since the surface of the sample is hydrophobic. The sphere adsorption begins immediately upon exposure of the substrate to the sphere suspension. The adsorption process is allowed to continue for about 1 hour. Then the sample is washed by a copious amount of deionized water to remove the non-adsorbed spheres on the surface. Subsequently the sample is dried in the air and the round boundary between the polystyrene sphere monolayer and the remaining Au surface can be clearly seen by eyes. Once dried, the spheres will be firmly adsorbed such that vigorous squirting of water from a wash bottle dislodged very few spheres. Finally both sides of the sample are completely dried using  $\text{N}_2$  flow.

### **4.2 Characterization of Au nanoshell film**

We fabricated Au nanoshell using different sizes of polystyrene spheres. To check on sample quality in terms of particle density and the monolayer formation, scanning electron microscope, atomic force microscope and conventional optical microscope are used to characterize the sample. We found that the appropriate mixture ratio for the sphere solution is a critical factor for successful formation of a polystyrene sphere monolayer. Spectrum analysis of the Au nanoshell film using a UV-VIS spectrometer is also performed in order to identify the scattering resonance peak.

#### **4.2.1 Imaging**

Samples prepared using the sphere solution with different mixture ratios are observed under SEM, as shown in Figure 4-3. As we can see from the five pictures, the density of

polystyrene spheres which are adsorbed on the Au surface is low when the concentration of EDC is equal to 0 and 16.7% (V/V) in the mixture solution (See Figure 4-3 (a) & (b)). The polystyrene spheres start clustering when the concentration of EDC is increased to 28.6% (V/V) in the mixture solution (See Figure 4-3 (d)). Figure 4-3 (c) shows a very good monodisperse layer of polystyrene spheres with dense distribution. This suggests that the appropriate ratio for the polystyrene sphere suspension, carbodiimide dissolved in phosphate buffer, and water is 1:2:2.

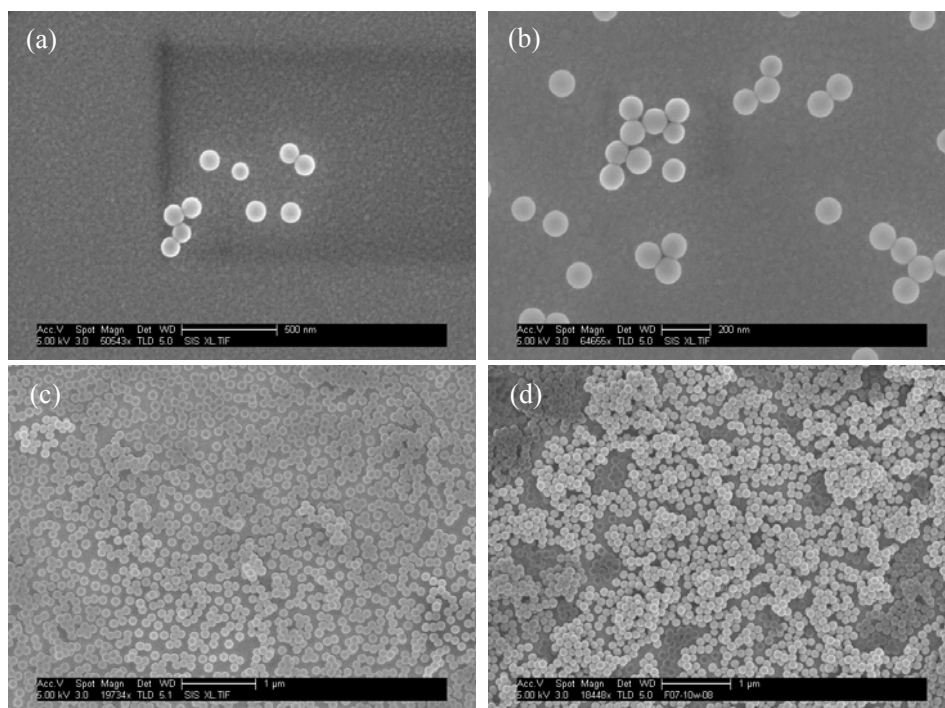


Figure 4-3 Scanning electron micrographs of Au nanoshell films prepared with the sphere solutions with different mixture ratios: (a) EDC: PS: H<sub>2</sub>O=0:1:1; (b) EDC: PS: H<sub>2</sub>O=1:3:2; (c) EDC: PS: H<sub>2</sub>O=1:2:2; (d) EDC: PS: H<sub>2</sub>O=1:1.5:1.

We can draw the conclusion from Figure 4-3 that: (1) Addition of EDC in the sphere suspension induces the adsorption of polystyrene spheres to the Au surface; (2) EDC also promotes the attraction between polystyrene spheres and excess EDC may cause the clustering of spheres. This indicates that the concentration of EDC slightly less than what is needed to initiate the agglomeration leads to the best result.

With a series of experiment, we are able to fabricate the Au-nanoshell films using different size of polystyrene sphere as the template, shown as follows.

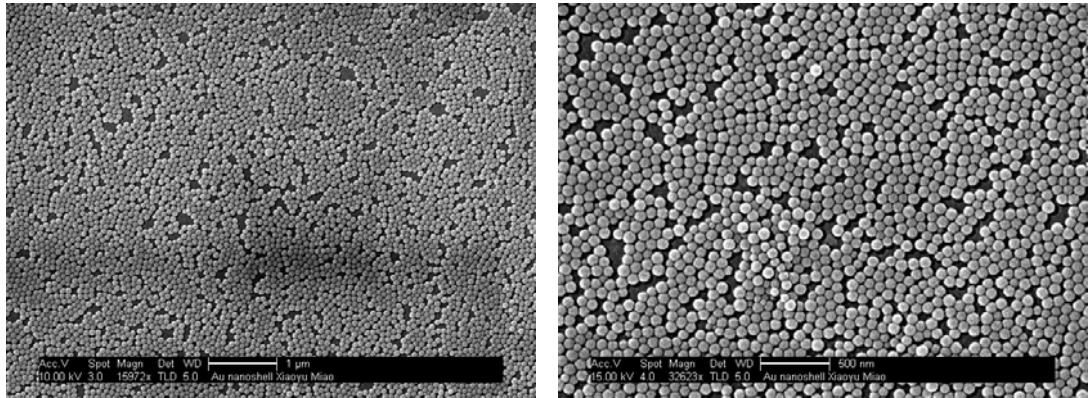


Figure 4-4 Au nanoshell film using polystyrene spheres (D=85 nm) as the template.

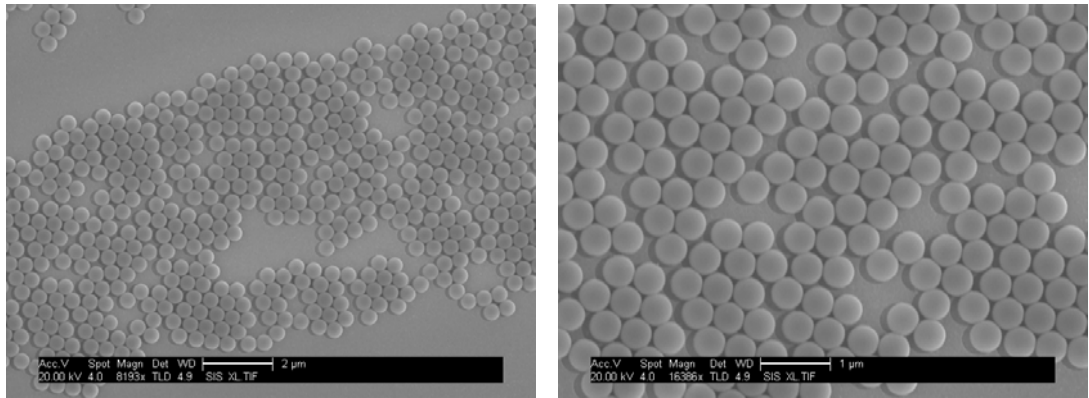


Figure 4-5 Au nanoshell film using polystyrene spheres (D=500 nm) as the template.

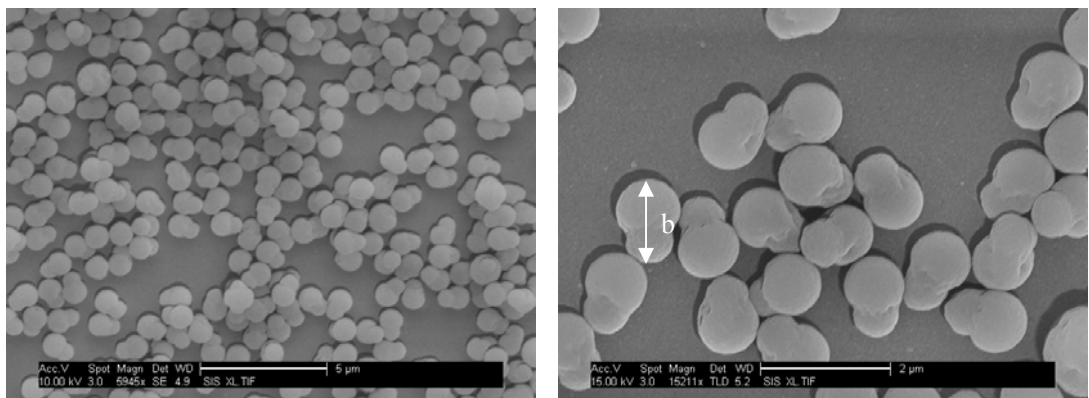


Figure 4-6 Au nanoshell film using polystyrene particles ( $a=1\ \mu\text{m}$ ,  $b=1.3\ \mu\text{m}$ ) as the template.

The polystyrene spheres with the diameter 85 nm in Figure 4-4 are monodisperse latex beads which are not modified with any functionalized group (Polysciences, Inc., Warrington, PA). The polystyrene spheres with the diameter 500 nm in Figure 4-5 are latex beads that contain surface carboxyl groups (Polysciences, Inc. Warrington, PA). Thus we can conclude that both the normal and functionalized polystyrene spheres can be used to in this fabrication approach. The polystyrene particles shown in Figure 4-6 are elliptical in shape (Spherotech Inc., Libertyville, IL). The length of the long axis and short axis are approximately  $1\ \mu\text{m}$  and  $1.3\ \mu\text{m}$  respectively. This provides us the ability to fabricate the Au nanoshell film with different shapes and study the influence to the localized surface plasmon resonance.

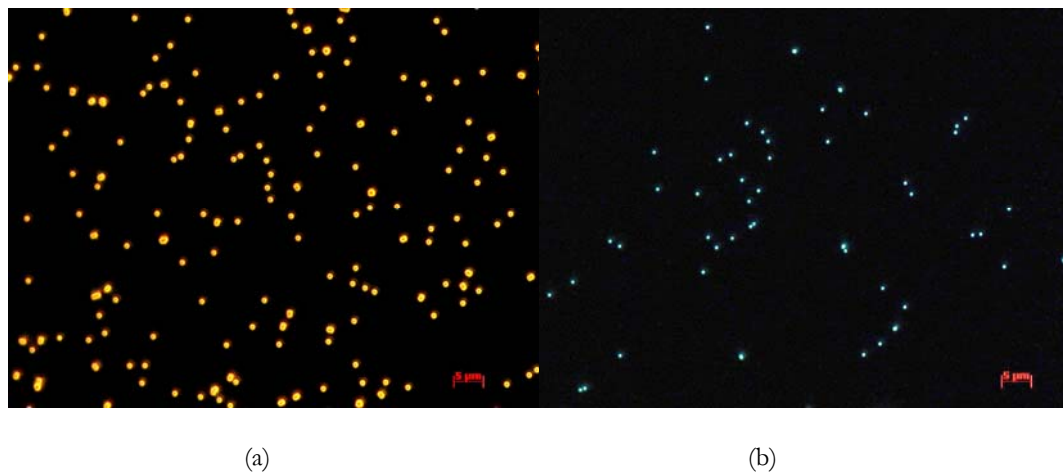


Figure 4-7 Optical microscope view of the Au nanoshell film under dark-field illumination (a) Polystyrene spheres ( $D=500\ \text{nm}$ ); (b) Polystyrene spheres ( $D=200\ \text{nm}$ )

Optical microscope is also utilized to image the sample under dark-field illumination in order to characterize its scattering property. To see the nanoparticles individually, we choose the sample with low density distribution. Figure 4-7 (a) & (b) show the view of the Au nanoshell film using polystyrene spheres with diameter  $D=500\ \text{nm}$  and  $D=200\ \text{nm}$  respectively. Both pictures are taken under the same illumination intensity. The comparison between the two pictures suggests that Au nanoshell with larger size has stronger scattering cross section which is consistent with conclusions found from references. By comparing to the visible spectrum shown in Figure 4-8, we can see that the scattering peak of the Au nanoshell film

fabricated with larger polystyrene spheres lies in longer wavelength region, which is also consistent with findings by other group.

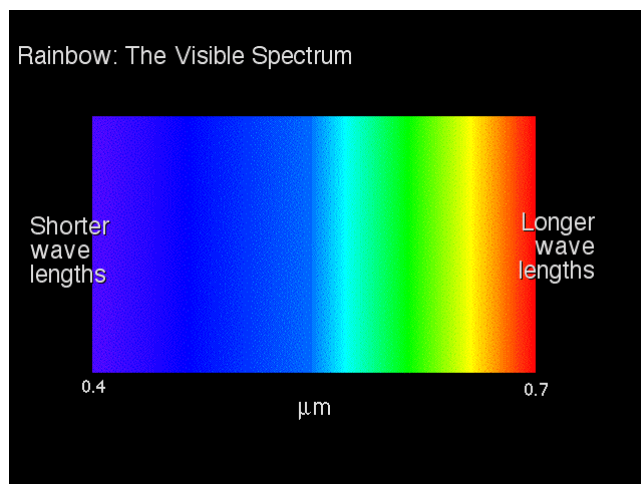
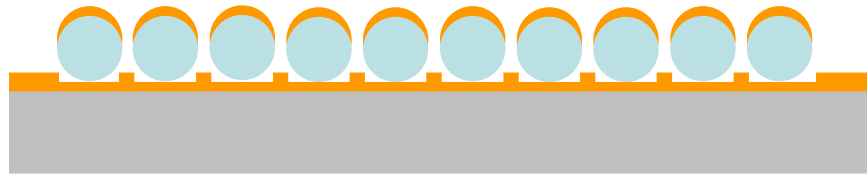
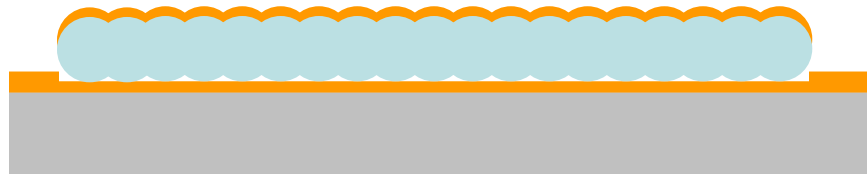


Figure 4-8 Electromagnetic spectrum of the visible light [121].

If the layer formed by the polystyrene spheres form is completely monodisperse, evaporation of Au on the template results in samples consisting of cap-shaped Au nanostructures, which are electrically isolated from the underlying Au film, shown in Figure 4-9 (a). Resulting Au nanostructures will be cap-shaped because the deposition of Au by thermal evaporation does not lead to coverage of the lower half of the adsorbed spheres. If the polystyrene spheres are clustering together (see Figure 4-3(d)), the second evaporated Au layer will interconnect without forming the isolated Au nanostructures, shown in Figure 4-7 (b). Atomic force microscope is used to explore the morphology of the sample when the template of polystyrene sphere layer shows clustering, which is shown in Figure 4-8. The maximum vertical range of the sample can be read from the chart which is only 8.61 nm. This value is much smaller than the diameter of the polystyrene sphere which is 85 nm for this sample. The sample is more like an Au film instead of a nanostructure. For the purpose of inducing strong localized surface plasmon resonance and further application for the Opto-Plasmonic Tweezers, the clustering of polystyrene spheres needs to be avoided by choosing appropriate concentration of EDC when preparing the sphere solution.

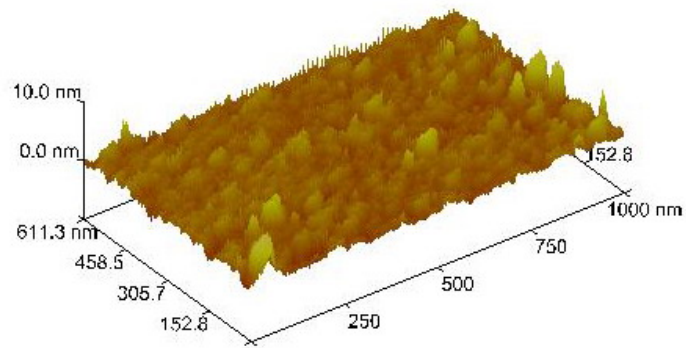


(a)

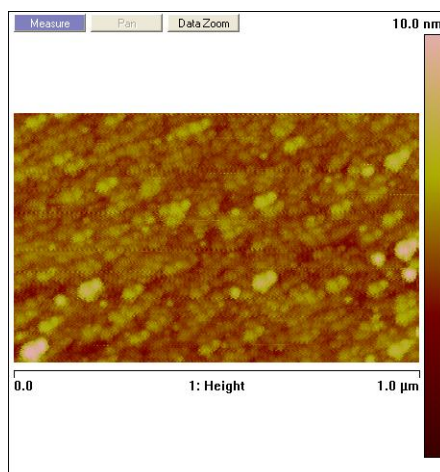


(b)

Figure 4-9 Morphology of the Au nanoshell film (a) when the polystyrene spheres are monodisperse; (b) when the polystyrene spheres are clustering.



(a)



(b)

Figure 4-10 AFM image of the sample when the self-assembled spheres are clustering (a) 3D; (b) 2D.

#### 4.2.2 Spectrum analysis

As shown in Figure 4-9, an epi-illumination fluorescence microscope (AXIO Imager DI from Zeiss) has been adopted as the platform for the spectrum measurement. The highly luminescent halogen light source of the microscope provides the broadband illumination required for absorption and scattering spectroscopy. The reflection and scattering light are then detected by a fiber-coupled CCD-based spectrometer (OSM-100, Spectra Physics, Mountain View, CA).

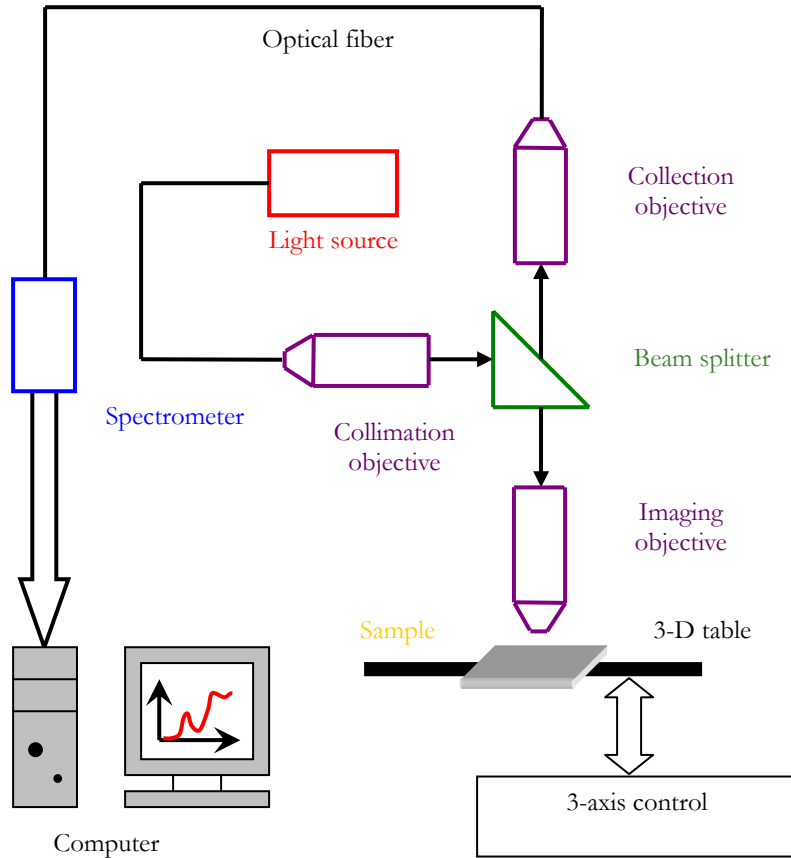


Figure 4-11 Schematic of the setup for measuring the reflection and scattering spectrum.

## Chapter 5 Conclusion

The Opto-Plasmonic Tweezers is proposed as a solution for manipulation of micro/nano particles. The chief motivation behind this work is to achieve not only trapping, but also rotation of the micro/nano particles. In addition to fine orientation control by adjusting the polarization direction of the incident light, the proposed approach is also expected to achieve lower optical intensity requirement than conventional optical tweezers.

To analyze the performance of the opto-plasmonic tweezers, theoretical model is developed to calculate the light induced dipole momentum, scattering field distribution, and the dielectrophoresis force exerted on micro/nano objects in both radial and angular directions. The results shows that the combination of radial and angular force will provide a stable trap for micro/nano objects, and align the long axis of an elongated object orthogonal to the polarization direction of the incident light. Finite element analysis is performed to calculate the magnitude of light induced dielectrophoresis force for a spherical object. Furthermore, 3D trapping trajectory is calculated which demonstrates that the micro/nano particles can be trapped and moved freely by adjusting the location of light beam. Next the model is expanded to simulate the light induced dielectrophoresis force and torque on non-spherical objects using *L. monocytogenes* as an example. The rotation behavior of the biological cell associated with the light induced dielectrophoresis torque is studied afterward.

Following the theoretical modeling discussion, the fabrication process and results of the Au nanostructure which is the key element to the whole approach, are presented. Au nanoshell film formatted using surface-adsorbed polystyrene spheres as a template is characterized by

SEM, AFM and optical microscope. The role of EDC for self assembly of polystyrene spheres is discussed according to a series of experimental results. After this, the reflection and scattering spectrum of the Au nanoshell film is then measured by a spectrometer in order to characterize the scattering peak and efficiency at the resonance.

For future theoretical work, improvement may be made by re-examining the scattering field from Au nanostructures under localized surface plasmon resonance happens by including the coupling between adjacent Au nanostructures. This will allow better characterization of the light induced dielectrophoresis force exerting on the micro/nano objects. In addition, numerical multipoles model will be adopted to calculate the light induced dielectrophoresis force and torque for micro/nano objects to give better estimation on the magnitude of the force and torque when the gradient of the electric field is comparable to the size of the object.

As for the fabrication aspects, another series of self-assembly experiment will be needed to search the condition to achieve the best monodisperse, dense distribution and large scattering cross sections for the Au nanoshell film. Further analysis to the spectrum measured will be necessary in order to estimate the scattering efficiency. We will also try to remove the polystyrene spheres layer after the second Au evaporation by sonicating the sample in ethanol solution and see whether this will improve and sharpen the resonance peak or not. Patterned Au nanoshell film using the same chemical assembly approach may be investigated for other applications such as plasmonic waveguide, etc.

Finally a bench-top optical system will be built to demonstrate the principle of the proposed approach. By adjusting the polarization of input laser light using a commercial polarization controller, the rotation of micro/nano objects suspended in an aqueous solution covering the Au nanostructure will be observed using the high-power fluorescence microscope. In addition, trapping and moving of the micro/nano objects will also be expected to be observed by moving the microscope stage relative to the focused light spot. The L-DEP force and torque under various input light intensities will be analyzed by measuring how fast the cell movement and rotation responding to the change in polarization and position of the light. The image of the sample under testing will be sent through the beam-splitter and collected by an imaging system attached to the microscope. The data collected by the

imaging system will be transmitted to a computer for force and torque analysis. It will also be used to calculate the resolution of orientation control. We will compare the experimental data with our simulation results, and improve our modeling by analyzing the discrepancy.

The proposed research can potentially lead to an instrument that combines the advantages of both optical tweezers and conventional DEP, with significantly lower optical intensity requirement compared to conventional optical tweezers and substantially higher resolution in orientation control compared to DEP. With the instrument, optical manipulation of biological cells with fine orientation control and high flexibility can be achieved. Such capability is essential to biological researches in cell collection, separation, concentration, and transportation, probing various force mechanisms in biological cells and DNAs, as well as biofilm growth and tissue engineering.

1. B. Sakmann, E. Neher, "*Single-Channel Recording*", Plenum Press, New York, 1995.
2. T. Strick, J. Allemand, V. Croquette, and D. Bensimon, "The Manipulation of Single Biomolecules," *Physics Today*, vol. 54, no. 10, Oct. 2001.
3. P. J. Burke, "Nanodielectrophoresis: Electronic Nanotweezers," *Encyclopedia of Nanoscience and Nanotechnology*. American Scientific, Stevenson Ranch, CA, 2004.
4. J. C. Ellenbogen, "A Brief Review of Nanoelectronic Devices," *Government Microelectronics Application Conference*, Mar. 1998.
5. R. Krupke, F. Henrich, H. B. Weber, M. M. Kappes, and H. v. Löhneysen, "Simultaneous Deposition of Metallic Bundles of Single-walled Carbon Nanotubes Using Ac-dielectrophoresis," *Nano Lett.*, vol. 3, no. 8, pp. 1019-1023, July 2003.
6. L. Dong, V. Chirayos, J. Bush, J. Jiao, V. M. Dubin, R. V. Chebian, Y. Ono, J. F. Conley, Jr., and B. D. Ulrich, "Floating-potential Dielectrophoresis-controlled Fabrication of Single-carbon-nanotube-transistors and Their Electrical Properties," *J. Phys. Chem. B*, vol. 109, pp. 13148-13153, June 2005.
7. B. Alp, J. S. Andrews, V. P. Mason, I. P. Thompson, R. Wolowacz, and G. H. Markx, "Building Structured Biomaterials Using AC Electrokinetics," *IEEE Engineering in Medicine and Biology*, vol. 22, no. 6, pp. 91-97, Nov./Dec. 2003.
8. C. E. Verduzco-Luque, B. Alp, G. M. Stephens, and G. H. Markx, "Constructing of Biofilms with Defined Internal Architecture Using Dielectrophoresis and Flocculation," *Biotechnol. Bioeng.*, vol. 83, pp. 33-34, July 2003.
9. S. Jovtchev, I. Djenev, S. Stoeff, and S. Stoylov, "Role of Electrical and Mechanical Properties of Red Blood Cells for Their Aggregation," *Colloids and Surfaces*, vol. 164, pp. 95-104, May 2000.
10. R. Dasgupta, S. K. Mohanty, and P. K. Gupta, "Controlled Rotation of Biological Microscopic Objects Using Optical Line Tweezers," *Biotechnol. Lett.*, vol. 25, pp. 1625-1628, Oct. 2003.
11. K. E. Drexler, "*Nanosystems: Molecular Machinery, Manufacturing , and Computation*," Wiley, New York, 1992.

12. R. Feynman, "*Microelectromechanical Systems*," reprinted from 1960 speech at Caltech, 1992.
13. X. Miao, H. Liao, and L. Y. Lin, "*Opto-Plasmonic Tweezers for Rotation and Manipulation of Micro/Nano Objects*," IEEE Optical MEMS, Oulu, Finland, 2005.
14. S. A. Maier, P. G. Kik, H. A. Atwater, S. Meltzer, E. Harel, B. E. Koel, and A. A. G. Requicha, "Local detection of electromagnetic energy transport below the diffraction limit in metal nanoparticle plasmon waveguides," *Nat. Mater.*, vol. 2, pp.229-232, 2003.
15. D. P. O'Neal, L. R. Hirsch, N. J. Halas, J. D. Payne, and J. L. West, "Photo-thermal tumor ablation in mice using near infrared-absorbing nanoparticles," *Cancer Letters*, vol. 109, pp. 171-176, 2004.
16. E. Hutter, and J. H. fendler, "Exploitation of localized surface plasmon resonance," *Adv. Mater.*, vol. 16, No. 19, 2004.
17. H. A. Pohl, "*Dielectrophoresis*," Cambridge University Press, Cambridge, UK, 1978.
18. T. B. Jones, "*Electromechanics of Particles*," Cambridge University Press, Cambridge, UK, 1995.
19. M. P. Hughes, "*Nanoelectromechanics in Engineering and Biology*," CRC Press, Boca Raton, 2003.
20. S. Masuda, M. Washizu, and T. Nanba, "Novel Method of Cell Fusion in Field Constriction Area in Fluid Integrated Circuit," *IEEE Trans. Indust. Appl.*, vol. 25, no. 4, pp. 732-737, July/Aug. 1989.
21. M. Washizu, T. Nanba, and S. Masuda, "Handling Biological Cells Using a Fluid Integrated Circuit," *IEEE Trans. Indust. Appl.*, vol. 26, no. 2, pp. 352-358, Mar./Apr. 1990.
22. R. Pethig, Y. Huang, X. B. Wang, and J. P. H. Burt, "Positive and Negative Dielectrophoretic Collection of Colloidal Particles Using Interdigitated Castellated Microelectrodes," *J. Phys. D: Appl. Phys.*, vol. 25, no. 5, pp. 881-888, May 1992.
23. G. H. Markx, M. S. Talary, and R. Pethig, "Separation of Viable and Non-viable Yeast Using Dielectrophoresis," *J. Biotechnol.*, vol. 32, pp. 29-37, Jan. 1994.
24. X. B. Wang, Y. Huang, J. P. H. Burt, G. H. Markx, and R. Pethig, "Selective Dielectrophoretic Confinement of Bioparticles in Potential Energy Walls," *J. Phys. D: Appl. Phys.*, vol. 25, no. 5, pp. 1278-1285, Aug. 1993.
25. G. H. Markx, P. A. Dyda, and R. Pethig, "Dielectrophoretic Separation of Bacteria Using

- a Conductivity Gradient,” *J. Biotechnol.*, vol. 51, pp. 175-180, Nov. 1996.
26. F. F. Becker, X. B. Wang, Y. Huang, R. Pethig, J. Vykoukal, and P. R. C. Gascoyne, “The Removal of Human Leukaemia Cells from Blood Using Interdigitated Microelectrodes,” *J. Phys. D: Appl. Phys.*, vol. 27, no. 12, pp. 2659-2662, Dec. 1994.
  27. M. Washizu, S. Suzuki, O. Kurosawa, T. Nishizaka, and T. Shinohara, “Molecular Dielectrophoresis of Biopolymers,” *IEEE Trans. Indust. Appl.*, vol. 30, no. 4, pp. 352-358, July/Aug. 1994.
  28. G. H. Markx, J. Rousselet, and R. Pethig, “DEP-FFF, Field-Flow Fractionation using Non-Uniform Electric Fields,” *J. Liq. Chromatogr. R. T.*, vol. 20, pp. 2857-2872, 1997.
  29. Y. Huang, X. B. Wang, F. F. Becker, and P. R. C. Gascoyne, “Introducing Dielectrophoresis As a New Force Field for Field-Flow Fractionation,” *Biophys. J.*, vol. 73, pp. 1118-1129, Aug. 1997.
  30. X. B. Wang, J. Yang, Y. Huang, J. Vykoukal, F. Becker, and P. R. C. Gascoyne, “Cell Separation by Dielectrophoretic Field-Flow-Fractionation,” *Anal. Chem.*, vol. 72, pp. 832-839, Feb. 2000.
  31. J. Cheng, E. L. Sheldon, L. Wu, A. Uribe, L. O. Gerrue, J. Carrino, M. J. Heller, and J. P. O Connell, “Preparation and Hybridization Analysis of DNA/RNA from *E. coli* on Microfabricated Bioelectronic Chips,” *Nat. Biotechnol.*, vol. 16, pp. 541-546, June 1998.
  32. Y. Huang, S. Joo, M. Duhon, M. Heller, B. Wallace, and X. Xu, “Dielectrophoretic Cell Separation and Gene Expression Profiling on Microelectronic Chip Arrays,” *Anal. Chem.*, vol. 74, pp. 3362-3371, July 2002.
  33. J. M. Yang, J. Bell, Y. Huang, M. Tirado, D. Thomas, A. H. Forster, R. W. Haigis, P. D. Swanson, R. B. Wallace, B. Martinsons, and M. Krihak, “An Integrated Stacked Microlaboratory for Biological Agent Detection with DNA and Immunoassays,” *Biosensors and Bioelectronics*, vol. 17, pp. 605-618, June 2002.
  34. T. Muller, A. M. Gerardion, T. Schnelle, S. G. Shirley, F. Bordoni, G. De Degasperis, R. Leoni, and G. Fuhr, “Trapping of Micrometre and Sub-micrometre Particles by High-Frequency Electric Fields and Hydrodynamic Forces,” *J. Phys. D: Appl. Phys.*, vol. 29, no. 2, pp. 340-349, Feb. 1996.
  35. M. G. Green, and H. Morgan, “Dielectrophoretic Separation of Nano-particles,” *J. Phys. D: Appl. Phys.*, vol. 30, no. 11, pp. L41-L44, June 1997.

36. M. P. Hughes, and H. Morgan, "Dielectrophoretic Trapping of Single Sub-Micrometre Scale Bioparticles," *J. Phys. D: Appl. Phys.*, vol. 31, no. 17, pp. 2205-2210, Sep. 1998.
37. M. P. Hughes, and H. Morgan, "Dielectrophoretic Characterization and Separation of Antibody-coated Submicrometer Latex Spheres," *Anal. Chem.*, vol. 71, pp. 3441-3445, Aug. 1999.
38. M. Washizu, and O. Kurosawa, "Electrostatic Manipulation of DNA in Microfabricated Structures," *IEEE Trans. Indust. Appl.*, vol. 6, pp. 1165-1172, Nov./Dec. 1990.
39. M. Washizu, O. Kurosawa, I. Arai, S. Suzuki, and N. Shimamoto, "Applications of Electrostatic Stretch-and-Positioning of DNA," *IEEE Trans. Indust. Appl.*, vol. 31, no. 3, pp. 447-456, May/June 1994.
40. H. Kabata, O. Kurosawa, I. Arai, M. Washizu, S. Margaron, R. Glass, and N. Shimamoto, "Visualization of Single Molecules of RNA Polymerase Sliding along DNA," *Science*, vol. 262, pp. 1561-1564, Dec. 1993.
41. N. Shimamoto, "One-Dimensional Diffusion of Proteins along DNA," *J. Bio. Chem.*, vol. 274, no. 22, pp. 15293-15296, May 1999.
42. S. Suzuki, T. Yamanashi, S. Tazawa, O. Kurosawa, and M. Washizu, "Quantitative Analysis of DNA Orientation in Stationary AC Electric Fields Using Fluorescence Anisotropy," *IEEE Trans. Indust. Appl.*, vol. 34, no. 1, pp. 75-83, Jan./Feb. 1998.
43. Y. Yamamoto, O. Kurosawa, H. Kabata, N. Shimamoto, and M. Washizu, "Molecular Surgery of DNA Based on Electrostatic Micromanipulation," *IEEE Trans. Indust. Appl.*, vol. 36, no. 4, pp. 1010-1017, July/Aug. 2000.
44. C. L. Asbury, and G. van den Engh, "Trapping of DNA in Nonuniform Oscillating Electric Fields," *Biophys. J.*, vol. 74, pp. 1024-1030, Feb. 1998.
45. C. L. Asbury, A. H. Diercks, and G. van den Engh, "Trapping of DNA by Dielectrophoresis," *Electrophoresis*, vol. 23, no. 16, pp. 2658-2666, Aug. 2002.
46. D. Porath, A. Bezryadin, S. de Vries, and CC. Dekker, "Direct Measurement of Electrical Transport through DNA Molecules," *Nature*, vol. 403, pp. 635-638, Feb. 2000.
47. C. Dekker, and M. A. Ratner, "Electronic Properties of DNA," *Phys. World*, vol. 14, Aug. 2001.
48. M. Washizu, S. Suzuki, O. Kurosawa, T. Nishizaka, and T. Shinohara, "Molecular Dielectrophoresis of Biopolymers," *IEEE Trans. Indust. Appl.*, vol. 30, no. 4, pp. 835-843,

July/Aug. 1994.

49. T. Kawabata, and M. Washizu, "Dielectrophoretic Detection of Molecular Bindings," *IEEE Trans. Indust. Appl.*, vol. 37, no. 6, pp. 1625-1633, Nov./Dec. 1998.
50. M. Washizu, M. Shikida, S. Arizawa, and H. Hotani, "Orientation and Transformation of Flagella in Electrostatic Field," *IEEE Trans. Indust. Appl.*, vol. 28, no. 5, pp. 1194-1202, Sep./Oct. 1992.
51. T. Schnelle, T. Muller, S. Friedler, S. G. Shirley, K. Ludwig, A. Herrmann, G. Fuhr, B. Wagner, and U. Zimmermann, "Trapping of Virus in High-Frequency Electric Field Cages," *Naturwissenschaften*, vol. 83, pp. 172-176, 1996.
52. H. Morgan, and N. G. Green, "Dielectrophoretic Manipulation of Rod-Shaped Viral Particles," *J. of Electrostat.*, vol. 42, pp. 279-293, Dec. 1997.
53. M. P. Hughes, H. Morgan, F. H. Rixon, J. P. H. Burt, and R. Pethig, "Manipulation of Herpes Simplex Virus Type I by Dielectrophoresis," *Biochim. Biophys. Acta*, vol. 1425, pp. 119-126, 1998.
54. H. Morgan, M. P. Hughes, and N. G. Green, "Separation of Submicron Bioparticles by Dielectrophoresis," *Biophys. J.*, vol. 77, pp.516-525, July 1999.
55. A. Bezryadin, and C. Dekker, "Nanofabrication of electrodes with sub-5 nm spacing for transport experiments on single molecules and metal clusters," *J. Vac. Sci. Technol. B*, vol. 15, pp. 793-799, 1997.
56. K. Yamamoto, S. Akita, and Y. Nakayama, "Orientation and purification of carbon nanotubes using ac electrophoresis," *J. Phys. D*, vol. 31, pp. L34-L36, 1998.
57. X. Q. Chen, T. Saito, H. Yamada, and K. Matsushige, "Align single-wall carbon nanotubes with an alternating-current electric field," *Appl. Phys. Lett.*, vol. 78, pp.3714-, 2001.
58. M. Dimaki, and Peter Bóggid, "Dielectrophoresis of carbon nanotubes using microelectrodes: a numerical study," *Nanotechnology*, vol. 15, pp.1095-1102, 2004.
59. R. Krupke, F. Hennrich, H. v. Lhneysen, M. M. Kappes, "Separation of metallic from semiconducting single-walled carbon nanotubes," *Science*, vol. 301, pp. 344-347, 2003.
60. M. R. Diehl, S. N. Yaliraki, R. A. Beckman, M. Narahona, and J. R. Heath, "Self-assembled, deterministic carbon nanotube wiring networks," *Angew. Chem. Int. Ed.*, vol. 41, pp. 353-356, 2002.

61. X. Duan, Y. Huang, Y. Cui, J. Wang and C. M. Lieber, "Indium phosphide nanowires as building blocks for nanoscale electronic and optoelectronic devices", *Nature*, vol. 409, pp. 66-69, 2001.
62. A. Ashkin, J. M. Dziedzic, and T. Yamane, "Observation of a single-beam gradient force optical trap for dielectric particles," *Opt. Lett.*, vol. 11, pp. 288-290, 1986.
63. S. M. Block, D. F. Blair, and H. C. Berg, "Compliance of bacterial flagella measured with optical tweezers," *Nature*, vol. 338, pp. 514-518, 1989.
64. K. Svoboda, and S. M. Block, "Biological applications of optical forces," *Ann. Rev. Biophys. Biomol. Struct.*, vol. 23, pp.247-285, 1994.
65. A. Ashkin, K. Schutze, J. M. Dziedzic, U. Euteneuer, and M. Schliwa, "Force generation of organelle transport measured in vivo by an infrared laser trap," *Nature*, vol. 348, pp. 346-348, 1990.
66. S. C. Kuo, and M. P. Sheetz, "Force of single kinesin molecules measured with optical tweezers," *Science*, vol. 260, pp. 232-234, 1993.
67. K. Svoboda, C. F. Schmidt, D. Branton, and S. M. Block, "Direct observation of kinesin stepping by optical trapping interferometry," *Nature*, vol. 365, pp. 721-727, 1993.
68. K. Svoboda, S. M. Block, "Force and velocity measured for single kinesin molecules," *Cell*, vol. 77, pp. 773-784, 1994.
69. H. Yin, M. D. Wang, K. Svoboda, R. Landick, S. M. Block, and J. Gelles, "Transcription against an applied force," *Science*, vol. 270, pp. 1653-1656, 1995.
70. M. Kurachi, M. Hoshi, and H. Tashiro, "Buckling of a single microtubule by optical trapping forces: Direct measurement of microtubule rigidity," *Cell Motil. Cytoskeleton*, vol. 30, pp. 221-228, 1995.
71. S. B. Smith, Y. Cui, and C. Bustamante, "Overstretching B-DNA: the elastic response of individual double-stranded and single-stranded DNA molecules", *Science*, vol. 271, pp. 795-799, 1996.
72. J. Dai, and M. P. Sheetz, "Mechanical properties of neuronal growth cone membranes studied by tether formation with laser optical tweezers," *Biophys. J.*, vol. 68, pp. 988-996, 1995.
73. R. C. Gauthier, "Theoretical investigation of the optical trapping force and torque on cylindrical micro-objects," *J. Opt. Soc. Am. B*, vol. 14, pp. 3323-3333, 1997.

74. R. C. Gauthier, M. Ashman, and C. P. Grover, "Experimental confirmation of the optical trapping properties of cylindrical objects," *Applied Optics*, vol. 38, pp. 4861-4869, 1999.
75. S. Sato, and M. Ishigure, "Optical trapping and manipulation of microscopic particles and biological cells using higher-order mode Nd:YAG laser beams," *Electron. Lett.*, vol. 27, pp. 1831-1832, 1991.
76. E. Higurashi, H. Uklata, H. Tanaka, and O. Ohguchi, "Optically induced rotation of anisotropic micro-objects fabricated by surface micromachining," *Appl. Phys. Lett.*, vol. 64, pp. 2209-2210, 1994.
77. A. Yamamoto, and I. Yamaguchi, "Measurement and control of optically induced rotation of anisotropic shaped particles," *Jpn. J. Appl. Phys.*, vol. 34, pp. 3104-3108, 1995.
78. H. He, M. E. J. Friese, N. R. hechenberg, and H. Rubinsztein-Dunlop, "Direct observation of transfer of angular momentum to adsorptive particles from a laser beam with a phase singularity," *Phys. Rev. Lett.*, vol. 75, pp. 826-829, 1995.
79. M. E. J. Friese, T. A. Nieminen, N. R. heckenberg, and H. Rubinsztein-Dunlop, "Optical alignment and spinning of laser-trapped microscopic particles," *Nature*, vol. 395, pp. 348-350, 1998.
80. E. Higurashi, R. Sawada, and T. Ito, "Optically induced angular alignment of trapped birefringent micro-objects by linearly polarized light," *Phys. Rev. E*, vol. 59, pp. 3676-3681, 1999.
81. E. Higurashi, R. Sawada, and T. Ito, "Optically driven angular alignment of microcomponents made of in-plane birefringent polyimide film based on optical angular momentum transfer," *J. Micromech. Microeng.*, vol. 11, pp. 140-145, 2000.
82. A. T. O'Neil, and M. J. Padgett, "Rotational control within optical tweezers by use of a rotating aperture," *Optics Lett.*, vol. 27, pp. 743-745, 2002.
83. A. Ashkin, and J. M. Dziedzic, "Optical trapping and manipulation of single living cells using infra-red laser beams," *Ber. Bunsenges. Phys. Chem.*, vol. 93, pp. 254-260, 1989.
84. K. C. Neuman, E. H. Chadd, G. F. Liou, K. Bergman, and S. M. Block, "Chracterization of photodamage to Escherorichia coli in optical traps," *Biophys. J.*, vol. 77, pp. 2856-2863, 1999.
85. P. Y. Chiou, A. T. Ohta, and M. C. Wu, "Massively parallel manipulation of single cells

- and microparticles using optical images,” *Nature*, vol. 436, pp. 370-372, 2005.
86. F. Ziemann, J. Padler, and E. Sackmann, “Local measurement of the viscoelastic moduli of entangled actin networks using an oscillating magnetic bead micro-rheometer,” *Biophys. J.*, vol. 66, pp. 2210-2216, 1994.
  87. F. Amblard, B. Yurke, A. N. Pargellis, and S. Leibler, “A magnetic manipulator for studying local rheology and micromechanical properties of biological systems,” *Rev. Sci. Instrum.*, vol. 67, pp. 1-10, 1996.
  88. C. Gosse, and V. Croquette, “Magnetic tweezers: Micromanipulation and force measurement at the molecular level,” *Biophys. J.*, vol. 82, pp. 3314-3329, 2002.
  89. N. Sundararajan, M. S. Pio, L. P. Lee, and A. A. Berlin, “Three-dimensional hydrodynamic focusing in polymethylsiloxane (PDMS) microchannels,” *J. of MEMS*, vol. 13, pp. 559-567, 2004.
  90. A. J. Haes, and R. P. Van Duyne, “A unified view of propagating and localized surface plasmon resonance biosensors,” *Anal. and Bioanal. Chem.*, vol. 379, pp. 920-930, 2004.
  91. J. Homola, S. Yee, and G. Gauglitz, “Surface plasmon resonance sensors: review,” *Sens. and Actuators B*, vol. 54, pp. 3-15, 1999.
  92. S. A. Maier, M. L. Brongersma, P. G. Kik, S. Meltzer, A. A. G. Requica, and H. A. Atwater, “Plasmonics – A route to nanoscale optical devices,” *Adv. Mater.*, vol. 13, pp. 1501-1505, 2001.
  93. P. C. Andersen, and K. L. Rowlen, “Brilliant optical properties of nanometric noble metal spheres, rods, and aperture arrays,” *Appl. Spectrosc.*, vol. 56, pp. 124A-135A, 2002.
  94. M. Kahl, E. Voges, S. Kostrewa, C. Viets, and W. Hill, “Periodically structured metallic substrates for SERS,” *Sens. and Actuators B*, vol. 51, pp. 285-291, 1998.
  95. G. C. Schatz, and R. P. Van Duyne, “*Electromagnetic mechanism of surface-enhanced spectroscopy*,” Wiley, New York, 2002.
  96. C. L. Haynes, and R. P. Van Duyne, “Plasmon-sampled surface-enhanced Raman excitation spectroscopy,” *J. Phys. Chem. B.*, vol. 107, pp. 7426-7433, 2003.
  97. Y. Dirix, C. Bastiaansen, W. Caseri, and P. Smith, “Oriented pearl-necklace arrays of metallic nanoparticles in polymers,” *Adv. Mater.*, vol. 11, pp. 223-227, 1999.
  98. C. L. Haynes, and R. P. Van Duyne, “Dichroic optical properties of extended nanostructures fabricated using angle-resolved nanosphere lithography,” *Nano Lett.*, vol.

- 3, pp. 939-943, 2003.
99. A. J. Haes, and R. P. Van Duyne, "A nanoscale optical biosensor: sensitivity and selectivity of an approach based on the localized surface plasmon resonance spectroscopy of triangular silver nanoparticles," *J. Am. Chem. Soc.*, vol. 124, pp. 10596-10604, 2002.
100. A. J. Haes, S. Zou, G. C. Schatz, and R. P. Van Duyne, "A nanoscale optical biosensor: the short range distance dependence of the localized surface plasmon resonance of silver and gold nanoparticles," *J. Phys. Chem. B*, vol. 108, pp. 6961-6969, 2004.
101. J.-M. Nam, C. S. Thaxton, and C. A. Mirkin, "Nanoparticle-based bio-bar codes for the ultrasensitive detection of proteins," *Science*, vol. 301, pp. 1884-1886, 2003.
102. U. Kreibig, and M. Vollmer, "*Cluster materials*," Springer Berlin, Heidelberg, New York, 1995.
103. B. T. Draine, and P. J. Flatau, "Discrete-dipole approximation for scattering calculations," *J. Opt. Soc. Am. A*, vol. 11, pp. 1491-1499, 1994.
104. Mie Plot computer program, available at: <http://www.philiplaven.com/mieplot.htm>.
105. C. A. Balanis, "*Advanced Engineering Electromagnetics*," John Wiley & Sons, 1989.
106. D. J. Griffiths, "*Introduction to electrodynamics*," Prentice Hall, New Jersey, 1999.
107. T. B. Jones, "Basic theory of dielectrophoresis and electrorotation," *IEEE EMBS Magazine*, vol. 22, pp. 33-42, 2003.
108. L. Lasa, P. Dehoux, and P. Cossart, "Actin polymerization and bacterial movement," *Biochimica et Biophysica Acta*, vol. 1402, pp. 217-228, 1998.
109. J. R. Robbins, A. I. Barth, H. Marquis, E. L. de Hostos, W. J. Nelson, and J. A. Theriot, "Listeria monocytogenes exploits normal host cells processes to spread from cell to cell," *J. Cell Bio.*, vol. 146, pp. 1333-1349, 1999.
110. J. A. Theriot, "The cell biology of infection by intracellular bacterial pathogens," *Annual Review of Cell and Development Biology*, vol. 11, pp. 213-239, 1995.
111. M. D. Welch, A. Iwamatsu, and T. J. Mitchison, "Actin polymerization is induced by Arp2/3 protein complex at the surface of Listeria monocytogenes," *Nature*, vol. 385, pp. 265-269, 1997.
112. J. A. Theriot, J. Rosenblatt, D. A. Portnoy, P. J. Goldschmidt-Clemons, and T. J. Mitchison, "Involvement of profilin in the actin-based motility of L. monocytogenes in

- cells and in cell-free extracts,” *Cell*, vol. 76, pp. 506-517, 1994.
113. L. A. Cameron, M. J. Footer, A. van Qudenaarden, and J. A. Theriot, “Motility of ActA protein-coated microspheres driven by actin polymerization,” *Proc. Natl. Acad. Sci. USA*, vol. 96, pp. 4908-4913.
114. A. Upadhyaya, J. R. Chabot, A. Andreeva, A. Samadani, and A. van Qudenaarden, “Probing polymerization forces by using actin-propelled lipid vesicles,” *Proc. Natl. Acad. Sci. USA*, vol. 100, pp. 4521-4526, 2003.
115. A. Upadhyaya, and A. van Qudenaarden, “Biomimetic system for studying actin-based motility,” *Curr. Biol.*, vol. 13, pp. R734-R744.
116. L. A. Cameron, J. R. Robbins, M. J. Footer, and J. A. Theriot, “Biophysical parameters influence actin-based movement, trajectory, and initiation in a cell-free system,” *Molecular Biology of the Cell*, vol. 15, pp. 2312-2323.
117. M. Nishioka, S. Katsura, K. Hirano, and A. Mizuno, “Evaluation of cell characteristics by step-wise orientational rotation using optoelectrostatic micromanipulation,” *IEEE Trans. Ind. Appl.*, vol. 33, pp. 1381-1387, 1997.
118. M. Himmelhaus, and H. Takei, “Cap-shaped gold nanoparticles for an optical biosensor,” *Sens. and Actuators B*, vol. 63, pp. 24-30, 2000.
119. H. Takei, “Surface-adsorbed polystyrene spheres as a template for nanosized metal particle formation,” *J. Vac. Sci. Technol. B*, vol. 17, pp. 1906-1911, 1999.
120. M. Himmelhaus, and H. Takei, “Self-assembly of polystyrene nano particles into patterns of random-close-packed monolayers via chemically induced adsorption,” *Phys. Chem. Chem. Phys.*, vol. 4, pp. 496-506, 2002.
121. Visible light spectrum: [Http://www.ems.psu.edu/courses/earth002/resources.html](http://www.ems.psu.edu/courses/earth002/resources.html).